SANDIA REPORT
SAND2011-9090
Unlimited Release
Printed December 2011

Microkinetic Modeling of Lean NO_x Trap Storage and Regeneration

Richard S. Larson, V. Kalyana Chakravarthy, Josh A. Pihl, C. Stuart Daw

Prepared by
Sandia National Laboratories
Albuquerque, New Mexico 87185 and Livermore, California 94550

Sandia National Laboratories is a multi-program laboratory managed and operated by Sandia Corporation, a wholly owned subsidiary of Lockheed Martin Corporation, for the U.S. Department of Energy's National Nuclear Security Administration under contract DE-AC04-94AL85000.

Issued by Sandia National Laboratories, operated for the United States Department of Energy by Sandia Corporation.

Available to DOE and DOE contractors from
U.S. Department of Energy
Office of Scientific and Technical Information
P.O. Box 62
Oak Ridge, TN 37831

Telephone: (865) 576-8401
Facsimile: (865) 576-5728
E-Mail: reports@adonis.osti.gov
Online ordering: http://www.osti.gov/bridge

Available to the public from
U.S. Department of Commerce
National Technical Information Service
5285 Port Royal Rd.
Springfield, VA 22161

Telephone: (800) 553-6847
Facsimile: (703) 605-6900
E-Mail: orders@ntis.fedworld.gov
Online order: http://www.ntis.gov/help/ordermethods.asp?loc=7-4-0#online

SAND2011-9090
Unlimited Release
Printed December 2011

Microkinetic Modeling of Lean NO_x Trap Storage and Regeneration

Richard S. Larson
Hydrogen and Combustion Technology Department
Sandia National Laboratories
P.O. Box 969
Livermore, CA 94551-0969

V. Kalyana Chakravarthy, Josh A. Pihl, and C. Stuart Daw
Fuels, Engines and Emissions Research Center
Oak Ridge National Laboratory
2360 Cherahala Blvd.
Knoxville, TN 37932-1563

Abstract

A microkinetic chemical reaction mechanism capable of describing both the storage and regeneration processes in a fully formulated lean NO_x trap (LNT) is presented. The mechanism includes steps occurring on the precious metal, barium oxide (NO_x storage), and cerium oxide (oxygen storage) sites of the catalyst. The complete reaction set is used in conjunction with a transient plug flow reactor code (including boundary layer mass transfer) to simulate not only a set of long storage/regeneration cycles with a CO/H_2 reductant, but also a series of steady flow temperature sweep experiments that were previously analyzed with just a precious metal mechanism and a steady state code neglecting mass transfer. The results show that, while mass transfer effects are generally minor, NO_x storage is not negligible during some of the temperature ramps, necessitating a re-evaluation of the precious metal kinetic parameters. The parameters for the entire mechanism are inferred by finding the best overall fit to the complete set of experiments. Rigorous thermodynamic consistency is enforced for parallel reaction pathways and with respect to known data for all of the gas phase species involved. It is found that, with a few minor exceptions, all of the basic experimental observations can be reproduced with the transient simulations. In addition to accounting for normal cycling behavior, the final mechanism should provide a starting point for the description of further LNT phenomena such as desulfation and the role of alternative reductants.

ACKNOWLEDGMENTS

The authors thank Dr. Andrew Lutz, formerly of Sandia, for initial development of the Chemkin-based transient plug flow reactor code (TPLUG). The efforts at Oak Ridge were sponsored by the US Department of Energy (DOE) under contract number DE-AC05-00OR22725 with the Oak Ridge National Laboratory (ORNL), managed by UT-Battelle, LLC. The contribution of Josh A. Pihl was supported in part by an appointment to the ORNL Postgraduate Research Associates Program, administered jointly by the Oak Ridge Institute for Science and Education and ORNL. Research at both Oak Ridge and Sandia was sponsored specifically by Gurpreet Singh and Ken Howden of the US DOE's Vehicle Technologies Program. Sandia is a multiprogram laboratory managed and operated by Sandia Corporation, a wholly owned subsidiary of Lockheed Martin Corporation, for the US DOE's National Nuclear Security Administration under contract number DE-AC04-94AL85000.

CONTENTS

FIGURES

TABLES

1. INTRODUCTION

Lean NO_x traps (LNTs) are among the top contenders for reducing NO_x concentrations in the exhaust from diesel and gasoline direct injection (GDI) engines. These aftertreatment devices have an inherent advantage over those based on selective catalytic reduction (SCR) in that the latter require NH_3, which is generated on board from thermolysis and hydrolysis of urea and thus requires additional hardware. In the past few years, hybrid LNT-SCR systems have been proposed [1–4] as a way of eliminating the need to carry urea for the SCR catalyst. In such systems, NH_3 generated and not consumed during the rich phase of LNT operation is stored and then used by the SCR catalyst to reduce any NO_x exiting the LNT. Whether used alone or within hybrid systems, LNTs clearly require more complex control strategies than do other aftertreatment devices, given that their operation inherently involves alternating between lean and rich conditions. A comprehensive model for LNT functioning can be a useful tool in understanding these catalysts and using them to best advantage. Such a model can also be the basis for developing more global models for use in system integration studies.

Models of various levels of complexity have been proposed in the past decade or so for simulating LNTs. These include simple control-oriented models [5–7], global kinetic models [8–14], and models attempting a detailed description of the surface chemistry [15–18]. It is no longer practical to give a brief survey of this growing field, which is the subject of a recent comprehensive review [19]. However, some key features of those papers most closely related to the present work should be mentioned here.

The NO_x storage model developed by Olsson et al. [15], which was later supplemented with propene-based regeneration kinetics [16], was shown to be quite accurate in predicting NO_2 uptake but could not account for NO uptake (in the presence of O_2) on $Pt/BaO/Al_2O_3$ [20]. This was due to the fact that storage in this model was limited by NO oxidation to NO_2. Lindholm et al. [17] have removed this limitation by assuming that NO can be directly adsorbed on both $BaCO_3$ and unidentified S_3 sites. Their rate equations suggest that NO adsorbs on both of these sites without the assistance of either a noble metal or gas phase oxygen. Experimental evidence suggests that NO can indeed adsorb on BaO/Al_2O_3 catalysts but that the rate and level of

adsorption are too low in the absence of O_2 or Pt [21–24]. Even when pretreatment is carried out in the presence of O_2, which could lead to formation of surface peroxides [25,26], BaO/Al_2O_3 formulations adsorb only a negligible amount of NO [22,23], suggesting that Pt plays a crucial role in NO uptake. Among other things, the present model attempts to show how NO can be taken up readily without being adsorbed directly on BaO or $BaCO_3$ sites.

Unlike the storage mechanism, the regeneration mechanism proposed by Lindholm et al. [17] is highly globalized, with reactions involving as many as twelve reactant molecules. Needless to say, this makes the assignment of reaction orders highly problematic. It should also be noted that thermodynamic consistency is not built into this mechanism, nor is it verified explicitly. This is understandable, however, because thermodynamic consistency is difficult to enforce when using non-mass-action kinetics. (The approach of Dumesic [27] cannot be considered completely rigorous, because it relies on steady state assumptions for reactive intermediates and invokes concepts from transition state theory. Furthermore, the analysis must be carried out on a case-by-case basis and would be unworkable for a very large reaction scheme.) The present model was designed to overcome this by using only reactions that can reasonably be treated as elementary, thereby allowing thermodynamic consistency to be imposed rigorously. This of course results in a somewhat larger reaction set, but most of the work involved in formulating the complex regeneration chemistry was carried out in a previous study [28]. The remaining task here was to construct a storage and release mechanism at a comparable level of detail and rigor.

To summarize, the purpose of this work was to develop a thermodynamically consistent microkinetic mechanism capable of describing all aspects of normal LNT functioning. This was done by starting with the precious metal mechanism reported earlier, augmenting it slightly, and then adding reactions relevant to the NO_x and oxygen storage sites. The kinetic parameters for all three phases were adjusted to provide the best possible fit to a large experimental data base consisting of both the steady flow temperature sweeps described previously [28] and long storage/regeneration cycles run at three distinct temperatures, as detailed below. The simulations of reacting flow in a monolith channel were carried out with a Chemkin-based transient plug flow reactor code. For completeness, gas phase (boundary layer) mass-transfer resistances were included in the simulations, although they were found to have little effect on the results.

Together, the one-dimensional reactor code and the multiphase reaction mechanism were found to be capable of reproducing nearly all of the experimental observations. Therefore, this likely represents the first truly microkinetic model that accounts successfully for the roles of both NO_x species (NO and NO_2), both principal reductants (CO and H_2), all three reduction products (N_2O, N_2, and NH_3), all major gas components (H_2O, CO_2, O_2, and N_2), and both principal kinds of storage (NO_x on BaO and O_2 on Ce_2O_3).

2. EXPERIMENTAL

2.1 Catalyst Samples

All experiments were performed on a commercial NO_x trap catalyst supplied by Umicore Autocat USA Inc. (Auburn Hills, MI). The samples were received as cylindrical flow-through monolith bricks (11.8 cm diameter, 15.2 cm long) containing square channels at a density of 100 cells/cm^2. The washcoat, which was specifically formulated for application with gasoline direct injection (GDI) engines, contained γ-Al_2O_3, BaO and ZrO_2-Ce_2O_3, along with 3.99 kg/m^3 of the noble metals Pt, Pd and Rh with relative masses 82:26:6, respectively. This particular NO_x catalyst has been selected by the LNT Focus Group of the DOE Crosscut Lean Exhaust Emissions Reduction Simulations (CLEERS) activity as a reference material for intersite collaboration (see www.cleers.org). Our experience with this GDI catalyst indicates that it exhibits the same basic trends in NO_x reduction behavior that are seen with other LNT catalysts, both model and commercial. Prior to experimentation, the catalyst brick was degreened in a furnace at 700°C for 16 hours under a flow of 10% water in air.

2.2 Flow Reactor Experiments

The apparatus, procedures, and results for the flow reactor experiments are described in detail elsewhere [29]. However, since the results from those experiments were used in mechanism development and are shown below as a basis for comparison with the simulation runs, we summarize the procedures here. Small cylindrical core samples (2.2 cm diameter, 1.3 or 7.6 cm long) were cut from the Umicore GDI catalyst brick and loaded into the flow reactor. Gas temperatures were measured with 0.5 mm diameter chromel/alumel thermocouples at locations 1 cm upstream of the catalyst, inside a monolith channel at the midpoint of the core sample, and 1 cm downstream of the catalyst. Outlet concentrations of NO and total NO_x were measured with chemiluminescent detectors (California Analytical Instruments Model 400-HCLD). An ammonia scrubber (Perma Pure model AS-200-08-SS) was installed upstream of the NO_x analyzers. Other catalyst outlet gas concentrations (NH_3, N_2O, CO, H_2O, and CO_2) were

measured with an FTIR spectrometer (Midac M2000 equipped with a Gemini Specialty Optics, 375 cm^3 volume, 3 m path length gas absorption cell).

All of the experiments were performed with N_2 as the balance gas, and all runs included 5% H_2O and 5% CO_2 to simulate exhaust conditions. Prior to each experiment, the catalyst was reduced for 30 minutes at 500°C under 0.1% H_2, 5% H_2O, and 5% CO_2. It was then cooled to the desired experiment operating temperature under 5% H_2O and 5% CO_2. Two distinct sets of experiments were run: steady flow temperature ramps and isothermal lean/rich cycles.

The steady flow temperature ramps were designed to isolate the NO_x reduction reactions occurring over the precious metal components of the LNT from the NO_x storage and release processes that take place during typical cyclical LNT operation. To achieve this, most of the experiments involved NO_x (either NO or NO_2) and a reductant (H_2, CO, or NH_3) flowing simultaneously over the catalyst. Subsidiary experiments to investigate secondary reactions in the channel, such as NH_3 oxidation and water-gas shift, were also conducted. At the beginning of each experiment, the catalyst was cooled to the starting temperature (100°C or somewhat lower) and reactant gas flows were initiated. Once the outlet concentrations stabilized, the catalyst temperature was ramped to 500°C at a rate of about 5°C/min. The temperature ramp experiments were conducted on a 1.3 cm long core sample under a total flow rate fixed to achieve a space velocity of 100,000 hr^{-1} based on total monolith volume and gas flows at standard temperature and pressure. A total of 21 steady flow temperature ramp experiments were performed; detailed discussions of all the runs can be found in our previous publications [28,29].

The second set of experiments held the catalyst temperature fixed while alternating the gas composition between lean and rich conditions through use of two separate gas manifolds fed to a solenoid-actuated four-way switching valve (Numatics MicroAir Series model M10SS600M000061). These experiments were intended to represent more closely the actual operation of an LNT while minimizing catalyst exotherms due to oxygen storage and NO_x reduction. A 7.6 cm long core sample was operated under a fixed flow rate to achieve a space velocity of 30,000 hr^{-1}, again based on total monolith volume and gas flows at standard

temperature and pressure. Each experiment consisted of three lean/rich cycles, with a 15 min lean phase and a 10 min rich phase. The lean phase gas composition consisted of 300 ppm NO, 10% O_2, 5% CO_2, and 5% H_2O (with the balance being N_2). During the rich phase, the feed gas included 625 ppm CO, 375 ppm H_2, 5% CO_2, and 5% H_2O. These cycling experiments were conducted at 200, 300, 400, and 500°C; however, runs at the latter temperature were not used in the data fitting process, partly due to the extreme computational cost of performing transient simulations at high temperatures.

3. MECHANISM DEVELOPMENT

The original intent of this study was to supplement the previously formulated mechanism describing chemistry on the precious metal sites [28] with reactions accounting for both NO_x and oxygen storage and release. This was based on the assumption that the steady-flow temperature sweep experiments used to generate the precious metal mechanism were in fact pseudo-steady and free of storage effects. Eventually it became clear that this assumption was only roughly correct, implying that the continued use of this mechanism unaltered would compromise the ability to model truly transient storage and regeneration processes. Therefore, the decision was made to re-evaluate the precious metal kinetic parameters (and even to alter the mechanism itself slightly) simultaneously with the main task of constructing the storage and release mechanisms. This obviously led to a substantial increase in the number of adjustable parameters. The computational effort was further increased by the fact that (a) it was deemed necessary to include the temperature sweeps along with the newer cycle experiments in the parameter fitting, and (b) it was necessary to simulate the temperature sweeps with a fully transient code. In short, the original two-tiered approach to mechanism construction was essentially replaced by a comprehensive one-step procedure, although the results reported earlier for the precious metal kinetics certainly provided a valuable starting point for the current work.

As finally implemented, then, the procedure for mechanism development was as follows. The precious metal chemistry from the earlier study was first carried over, with the kinetic parameters once again being considered unknown and a few slight changes being made to the reaction set itself. Candidate reactions for the NO_x and oxygen storage sites were then added. These were constructed largely on the basis of suggestions in the literature, although it was often necessary to rewrite these to be consistent with our policy that all reactions be elementary enough to be represented by mass-action kinetics. Published kinetic parameters for reactions in this form were rarely available and would in any case be of questionable applicability due to differences in catalyst formulation; therefore, parameters for these reactions were also treated as adjustable, as were the effective (Chemkin-based) site densities for the three active phases of the catalyst. Obviously, the total number of adjustable parameters at this point was quite large. However, the number was reduced considerably by applying a set of rigorous thermodynamic

constraints. These guaranteed consistency with regard to the thermodynamics of parallel reaction paths and also ensured that the known properties of all gas-phase species were incorporated. All activation energies, whether varied freely or determined by a thermodynamic constraint, were in addition required to be non-negative. The set of activation energies was further constrained by requiring all molecular (non-dissociative) adsorptions on the precious metal sites to have negative enthalpy changes.

For the candidate mechanism thus constructed, the main task was to optimize the set of kinetic parameters (and site densities) relative to a suitable experimental data set. Clearly, a large number of parameters requires a very large amount of data. As noted previously, we elected to fit simulation results simultaneously to all 21 of the temperature ramps and all three of the long cycle experiments discussed above. If successful, this would demonstrate that the mechanism could account for LNT behavior over a very wide variety of conditions. For each type of experiment, the simulation was carried out with an in-house Chemkin-based transient plug flow reactor code. Thus, temporal and axial variations in the monolith channel could be accounted for with complete generality. Furthermore, even though the simulations were mathematically one-dimensional, radial mass transfer through the gas-phase boundary layer was accounted for via the use of standard mass transfer coefficients and two sets of gas-phase concentrations (surface and bulk). On the other hand, transport within the solid (washcoat) phase was not included explicitly in the calculations, so any effects connected with this must be regarded as being lumped into the kinetics.

The task of actually carrying out the parameter optimization was handled by the Sandia-developed APPSPACK code [30]. The objective function was an overall root-mean-square deviation between the simulated and measured outlet concentrations for the five gas-phase species of primary interest (NO, NO_2, N_2O, NH_3, and CO). The storage/regeneration cycles, taken as a group, were weighted equally with the temperature ramps, apart from a factor that accounted for the difference between the typical inlet NO_x concentrations. The efficiency of the optimization was enhanced by two techniques that served to decouple the parameters to some extent. The first was the well-known temperature-centering procedure, which partially insulates a rate constant from changes in its activation energy. The second was designed to decouple the

reaction rate from the site density by scaling the rate constant according to the mass-action law for the reaction. As a result of this, changes in the site density affected only the capacity of the phase in question.

Even with these improvements, the computation time required to carry out an optimization was considerable. Typically, finalizing the parameters for a given candidate mechanism consumed several days when running with 80 processors on a parallel machine. However, the most relevant issue was not the time required per mechanism, but rather the number of different mechanisms arising from the various combinations of candidate reactions.

4. SIMULATION DETAILS

Simulations of both the temperature ramp experiments and the storage/regeneration cycles were carried out with the transient plug flow reactor code TPLUG, which uses the Chemkin software package [31] to handle the chemistry. In TPLUG, the governing equations are discretized in the spatial (axial) direction, and the resulting differential-algebraic system is integrated in time with the DASAC software [32]. The set of governing equations consists of an overall continuity equation for the gas, material balances for all of the gas-phase and surface species, an ideal gas equation of state, and flux balances for the gas-phase boundary layer. An energy equation was deemed not to be necessary in this study, because experimental temperatures as a function of time were available as input, and measurements showed that axial variations were small. In any case, it is unlikely that internal temperature gradients could have been predicted with sufficient accuracy to be useful in the parameter estimation process. The pressure was even less likely to vary axially than was the temperature, so a momentum equation was also unnecessary.

The equations solved in this basic version of TPLUG can be summarized as follows. First, the gas phase continuity equation is expressed in the form

$$A_c \frac{\partial \rho}{\partial t} = -\frac{\partial}{\partial x}\left(\rho u A_c\right) + a_i \sum_{\text{gas}} s_k M_k \tag{1}$$

where t and x are the time and spatial variables, ρ is the mass density of the gas, u is the axial velocity, A_c is the cross-sectional area of the channel, a_i is the nominal surface area per unit length, M_k is the molecular weight of species k, and s_k is the molar production rate of this species per unit area. The corresponding material balance for gas-phase species k is

$$A_c \rho \left(\frac{\partial Y_k}{\partial t} + u \frac{\partial Y_k}{\partial x} \right) = M_k \left(s_k a_i + g_k A_c \right) - a_i Y_k \sum_{\text{gas}} s_j M_j \tag{2}$$

where Y_k is the mass fraction of this species and g_k is its molar production rate per unit volume by homogeneous gas reactions. Of course, g_k is identically zero for the purely catalytic process under study here. It must be emphasized, though, that in general g_k is evaluated at the bulk gas-phase composition, while s_k is evaluated at the surface, i.e., the inner edge of the gas-phase

boundary layer. The compositions at the two locations are related by a set of flux balances of the form

$$s_k = \lambda_k \left(c_{k,s} - c_k \right) \tag{3}$$

where λ_k is the mass-transfer coefficient for species k, c_k is its molar concentration, and the subscript s denotes surface conditions. λ_k is calculated from the assumption that the Sherwood number is constant at an asymptotic value of 3:

$$\lambda_k = \frac{3D_k}{d} \tag{4}$$

where D_k is the diffusivity of species k in the bath gas and d is the equivalent diameter of the channel [33]. The value of 3 is merely an approximation, given that the washcoated channel is not truly square in cross section [34]. In accordance with standard practice, the temperature dependence of the diffusivity is taken to be a simple power law:

$$D_k = D_{k,r} \left(\frac{T}{T_r} \right)^{1.75} \tag{5}$$

where $D_{k,r}$ is the value at an arbitrary reference temperature T_r, chosen in TPLUG as 573.15 K.

Clearly, Eq. (3) is not applicable to the bath gas species, for which the appropriate substitute relation is simply

$$\sum_{\text{gas}} Y_{k,s} = 1 \tag{6}$$

The ideal gas law, which is used to calculate the concentrations in Eq. (3), also provides the equation of state for the bulk gas:

$$PM = \rho RT \tag{7}$$

where P is the absolute pressure, M is the average molecular weight of the mixture, and R is the universal gas constant. The final block of equations solved by TPLUG consists of material balances for the surface species. Because there is assumed to be no transport on the surface, these equations take the simple form

$$\frac{\Gamma}{\sigma_k} \frac{\partial Z_k}{\partial t} = s_k \tag{8}$$

where Γ is the site density of the surface phase in question, Z_k is the site fraction of species k in this phase, and σ_k is the site occupancy number (i.e., the number of sites covered per admolecule) for this species.

An important consideration in carrying out the cycle simulations was selecting the proper initial conditions, given the significant capacity of the storage materials. Because the experimental cycles (three in all at each temperature) were shown to be highly repeatable, it was logical to impose a periodicity or self-consistency condition on the simulations, meaning simply that the state of the system at the end of a full cycle was forced to match that at the beginning. This required a certain amount of iteration, but a simple successive substitution approach was found to be adequate. Initial conditions for the temperature ramps were thought not to be as crucial, given that storage effects were minimized by design in these experiments. Still, the conditions were specified as accurately as practical by simulating the experimental pretreatment regimen [34] with a preliminary but reasonably refined version of the mechanism. This led to a precious metal (nominally platinum) surface consisting of about 19% vacant sites and 81% adsorbed H_2O, a BaO surface comprising 98% carbonate and 2% bare oxide, and a cerium oxide surface with no stored oxygen.

The specification of time-dependent inlet conditions for the cycles was complicated slightly by the need to satisfy the above-mentioned periodicity conditions. Thus, rich inflow conditions were actually in effect at $t = 0$, with a switch to lean flow being made very shortly thereafter, and a switch back to rich flow taking place just after $t = 900$ s. In order to avoid possible numerical difficulties caused by instantaneous flow transitions, a hyperbolic tangent function was used to spread each transition over a finite interval of about 1 s.

The (spatially uniform) temperatures used in the cycle simulations were the time-dependent values measured at the channel exit rather than the nominal values. Thus, even though the experiments were intended to be isothermal, they were not treated as such in the simulations. However, due to the low reductant concentrations used, the temperature rise during the rich phase was only about 6°C in all three cases. Therefore, the driving force for NO_x desorption was clearly not thermal, but rather the abrupt change in the chemical composition of the gas phase.

Minimizing temperature excursions, which can be difficult to measure or predict, was key to improving the reliability of the extracted kinetic parameters.

Also in the interest of accuracy, the temperature ramp rates used in simulating the steady flow experiments were the as-recorded values rather than the single nominal value of 5°C/min. In addition, modest adjustments of some of the experimental outlet gas concentrations for the cycles were carried out. Specifically, for the three species (CO, NH_3, and N_2O) whose concentrations were measured by FTIR, the values were time-smoothed and then corrected for time lags in the FTIR instrument, using a cell residence time of about 7 s.

5. REACTION MECHANISM

The final mechanism resulting from many iterations of the development process is summarized in Table 1. This involves the same ten gas-phase species considered in our previous paper (O_2, NO, NO_2, CO, H_2, CO_2, N_2, H_2O, N_2O, and NH_3) as well as surface species residing on one of three surface phases (or site types), nominally Pt, BaO, and Ce_2O_3.

As before, the precious metal phase is referred to as platinum, with the understanding that this really accounts for the palladium and rhodium components as well. This phase is assumed to be populated by 14 distinct species: V(Pt), O(Pt), NO(Pt), NO_2(Pt), CO(Pt), H(Pt), N(Pt), OH(Pt), H_2O(Pt), NH(Pt), NH_2(Pt), NCO(Pt), NH_3(Pt), and N_2O(Pt). All but the last of these have been carried over from our earlier study, although the notation has been changed; in particular, V is now used to refer to a vacant site.

The NO_x storage phase is considered to be BaO, even though it is widely acknowledged that NO_x can be stored on other components in a fully formulated catalyst. The six species populating this phase are BaO, $BaCO_3$, BaO–O, BaO–NO_2, BaO–NO_3, and $Ba(NO_3)_2$. The first of these is simply an oxygen-terminated site that shares a name with, but is otherwise distinct from, the BaO storage phase. The presence of $BaCO_3$ is assured in any system containing realistic amounts of CO_2; on the other hand, we have chosen not to include $Ba(OH)_2$, in part because it is less stable than the carbonate, but also because the roles of the two species could probably not be distinguished, given the unvarying levels of CO_2 and H_2O. The final four species are those that appear in conventional descriptions of NO_x storage [15], although other candidates have been proposed [35]. Because these are true surface species, they need not adhere to any conventional bulk stoichiometry, but the inclusion of the stoichiometric nitrate $Ba(NO_3)_2$ makes it possible to write some overall (global) reactions for the NO_x storage process. Yet, even this entity is treated as a surface rather than bulk species in the Chemkin formulation, primarily to ensure that the NO_x storage capacity is a fixed, finite number.

Finally, the oxygen storage capability of the catalyst is implemented via the two species Ce_2O_3 and Ce_2O_4, the latter being a convenient alternative designation for the more conventional CeO_2.

With this formulation, there is no need to be concerned with site occupancy numbers, as each pair of cerium atoms is considered to be a single site for oxygen atom adsorption.

The reactions listed in Table 1 fall naturally into four groups, namely those occurring exclusively on Pt sites, those occurring on BaO sites, spillover reactions involving species on both Pt and BaO, and spillover reactions involving Pt and Ce_2O_3. The Pt reactions are carried over almost intact from our previous paper, with most of the exceptions involving the relatively minor species N_2O. In the current mechanism, the synthesis and decomposition of N_2O take place only through the newly introduced adsorbed form, and there is of course a new reaction accounting for adsorption and desorption. There is also a new reaction describing the formation of N_2O(Pt) from NO(Pt) and NH(Pt), while the analogous reaction involving NO(Pt) and N(Pt) has been deleted. These changes were made largely in an attempt to solve one of the most difficult puzzles connected with the experimental temperature ramp data, namely that oxidation of NH_3 produces substantial amounts of N_2O, while reduction of N_2O produces no NH_3, even with a large excess of reductant. It is tempting to suggest that the N-N bond cannot be broken once formed, thus accounting for the second observation, but application of thermodynamic constraints to these reversible reactions seems to imply that the reverse (synthesis) process will then not occur either. A large amount of effort in this study was devoted to addressing this open question, but without complete success.

The storage/release reactions occurring on the BaO phase are comparatively small in number. The first is actually the only step in the entire mechanism that involves $BaCO_3$, and it simply allows CO_2 to compete with NO_x for available storage sites. The direct displacement of NO_x by CO_2 [36] could have been used instead (or in addition), but this was found not to be advantageous. Reactions (S29)–(S32) constitute a NO_x storage mechanism that is similar to that of Olsson et al. [15], but with two principal differences. Specifically, while (S29) and (S32) have exact analogs in that paper, (S30) and (S31) do not. However, (S30) is just a combination of (S29) and a reaction that appears in [15] but not here, namely

$$BaO–NO_2 = BaO–O + NO \quad (9)$$

Likewise, (S31) is the sum of (9) and another reaction from [15]:

$$NO_2 + BaO–O = BaO–NO_3 \quad (10)$$

The combined reactions simply allow the exchange of NO_2 for NO to take place in a single step. Alternatively, they can be regarded as expressing the ability of NO_2 to oxidize species residing on the BaO surface (or of NO to reduce them). In short, the storage mechanism used here is basically consistent with that in [15], but it has been reconfigured in order to provide the best match to the experimental data.

The spillover reactions in Table 1 are by definition those that involve a direct interaction between species on two distinct surface phases. Specifically, they allow for the direct oxidation, reduction, or decomposition of species on the storage sites by reactants residing on adjacent precious metal sites. Each of these reactions provides a one-step pathway for a process that could otherwise occur via a sequence of steps, each involving only a single surface phase. It has been widely speculated that some of the processes occurring in LNTs are strongly affected by the proximity of precious metal and storage sites, and the use of these spillover reactions is designed to account for that. However, because our reactor model does not include surface transport of reactive species, the effects of such transport must be regarded as being lumped into the corresponding rate constants. A reaction somewhat similar to (S34) is used by Lindholm et al. [17]. The same reference postulates a number of spillover reactions for the reduction of stored NO_x, but these are far from elementary.

It should be noted that the only reductants to be involved directly in Pt-BaO spillover reactions in the current mechanism are CO(Pt) and H(Pt), the latter having been considered previously [37–39]. By contrast, NH_3 can release stored NO_x only by first decomposing on Pt to produce H(Pt), even though the direct involvement of NH_3(Pt) in such spillover reactions has been suggested, at least globally [14,17]. Despite this possible oversimplification, NH_3 production at the regeneration front and its subsequent consumption downstream [40] appear to be well captured by the current model.

Reaction (S44) provides a very simple way to account for oxygen storage on the cerium oxide phase. While this process has been studied extensively in connection with its role in three-way catalysis [41], it has not often appeared in models of LNT chemistry, largely because model LNT catalysts are typically formulated without an oxygen storage component. Nevertheless, our

simulations of storage/regeneration cycles show this process to be of crucial importance with the commercial Umicore catalyst, as has been conjectured [42]. The treatment of oxygen storage as a spillover reaction rather than a direct dissociative adsorption of molecular O_2 is consistent with the corresponding process on the BaO phase, namely reaction (S33). It is likewise consistent with suggestions appearing in the literature [43,44]. By contrast, this level of detail is unavailable in the global kinetic model of Koci et al. [14].

The final reaction in Table 1 is similar in spirit to those occurring exclusively on Pt sites, but it uses oxygen from a ceria site to allow the reductant NH_3(Pt) to be fully oxidized. As will be shown below quantitatively, this somewhat complex reaction is not essential for simulating the temperature ramp and long cycle experiments used here in parameter estimation, but it *is* crucial in preventing excessive NH_3 production during the much shorter cycles typically used in practice.

Table 1 also gives the forward and reverse kinetic parameters for each reaction, i.e., the values of A, n, and E in the generalized Arrhenius expression

$$k = AT^n \exp\left(-E/RT\right) \tag{11}$$

Those reactions indicated as being part of the core set form a complete, linearly independent basis set with respect to the surface species, whose thermodynamic properties are unknown. For each such reaction, the equilibrium constant was free to vary during the optimization process, so the pre-exponential factors and activation energies in both directions were adjustable, subject to the decoupling procedures discussed earlier. For these reactions, the temperature exponents were set identically to zero. For each of the non-core reactions, the equilibrium constant was subject to a thermodynamic constraint, so the kinetic parameters in only one direction could be varied freely, the temperature exponent again being set to zero. Kinetic parameters in the other direction were then fixed by the constraint, and a nonzero temperature exponent could arise from the incorporation of known thermodynamic properties for gas-phase species.

Reactions that are so fast as to be at equilibrium present a special problem for the optimization procedure used here. For any such reaction, the kinetic parameters are to some extent indeterminate, because proportionate increases in the forward and reverse rate constants produce

no change in the simulated results. The best that can be done in such a case is to establish lower bounds on the pre-exponential factors. There is a practical advantage to identifying and using those bounds, because unnecessarily fast reactions produce excessive stiffness and thereby slow down the computations. Of course, a lack of sensitivity to the rate constants can also mean that the reaction itself is not very important, and in that case an assessment of equilibrium is not worthwhile. For the mechanism in Table 1, it is found that reactions (S1), (S4), (S7), (S15), and (S18) are crucial to the simulations (as will be detailed later) and also fast enough to be at equilibrium. Thus, the corresponding rate parameters are not as well-determined as the others in the table.

Table 2 lists the thermodynamic consistency relations, which express each of the non-core reactions as a linear combination of core surface reactions and members of a corresponding set of core gas reactions. The way in which these equations are translated into relations between the forward and reverse kinetic parameters is detailed elsewhere [28] and need not be repeated here. The gas reactions appearing in the consistency relations are summarized in Table 3 along with their equilibrium constants (in the concentration units needed for the constraints) expressed in the form

$$K = K_0 T^n \exp\left(-Q/RT\right) \tag{12}$$

It should be emphasized that these gas reactions are *not* a part of the reaction mechanism, which consists entirely of the surface reactions appearing in Table 1. However, the gas reactions play an essential role in assuring that the surface mechanism is consistent with known thermodynamics.

Finally, it must also be emphasized that the pre-exponential factors in Table 1 are meaningless without a specification of the site densities for the three surface phases. The values obtained from the optimization, expressed in $\mathrm{mol/cm^2}$ of nominal surface, are 8.095×10^{-8}, 8.846×10^{-7}, and 1.971×10^{-6} for the Pt, BaO, and Ce_2O_3 phases, respectively. For any changes in these values, the pre-exponential factors could be scaled according to the respective reaction orders (in line with mass-action kinetics) in such a way as to leave the reaction rates unchanged. However, the storage capacities of the phases would be altered, so the site densities cannot be regarded as

arbitrary, as was the case previously [28]. This is clearly just a consequence of dealing with transient rather than steady or pseudo-steady processes.

Because the formulation of the commercial Umicore catalyst is not known in detail, it is difficult to obtain independent estimates of the three site densities. However, it is possible to show that the value inferred for the Pt phase is reasonable. Together, the overall precious metal loading of 3.99 kg/m^3 and the channel density of 100 cm^{-2} imply that the washcoat in a single channel contains 3.99×10^{-5} g of metal per cm of length. Using an effective channel diameter of 0.119 cm, this translates to a loading of 1.07×10^{-4} g for every cm^2 of nominal surface area. The average molecular weight of the three metals is about 158, so the loading in molar units is roughly 6.8×10^{-7} mol/cm^2. This is a factor of about 8.4 larger than the inferred site density, which is at least qualitatively consistent with the premise that only a fraction of the atoms in a metal cluster are actually accessible to the gas-phase reactants.

Table 1. Reactions in the surface mechanism and the corresponding kinetic parameters. An asterisk indicates a core reaction.

No.	Reaction	*A* (cgs units)	*n*	*E* (kJ/mol)
Reactions on precious metal (Pt) sites:				
(S1)*	NO + V(Pt) = NO(Pt)	3.890E+13	0	27.59
		6.641E+12	0	73.45
(S2)*	NO_2 + V(Pt) = NO_2(Pt)	3.530E+10	0	19.22
		6.806E+13	0	96.76
(S3)*	CO + V(Pt) = CO(Pt)	2.961E+21	0	100.62
		1.191E+14	0	100.62
(S4)*	H_2O(Pt) = H_2O + V(Pt)	2.992E+12	0	87.07
		5.071E+13	0	53.83
(S5)*	NH_3 + V(Pt) = NH_3(Pt)	6.192E+29	0	183.14
		8.229E+28	0	203.44
(S6)*	O_2 + 2V(Pt) = 2O(Pt)	4.776E+24	0	58.39
		2.070E+29	0	182.81
(S7)*	H_2 + 2V(Pt) = 2H(Pt)	1.058E+23	0	51.93
		8.436E+21	0	81.06
(S8)	CO(Pt) + O(Pt) = CO_2 + 2V(Pt)	3.308E+12	0	0.00
		1.597E+21	–0.4874	221.36
(S9)	2N(Pt) = N_2 + 2V(Pt)	6.092E+16	0	91.88
		7.915E+11	0.0482	125.96
(S10)	NO(Pt) + NH(Pt) = N_2O(Pt) + H(Pt)	1.136E+12	0.6092	47.13
		3.404E+20	0	41.70
(S11)	2N(Pt) + O(Pt) = N_2O(Pt) + 2V(Pt)	1.714E+33	0	174.37
		1.760E+30	–0.6092	65.18
(S12)*	NO(Pt) + V(Pt) = N(Pt) + O(Pt)	9.392E+18	0	85.01
		1.209E+25	0	174.58
(S13)	NO(Pt) + O(Pt) = NO_2(Pt) + V(Pt)	2.048E+27	0.2231	184.22
		1.523E+31	0	210.69

(S14)	$H(Pt) + OH(Pt) = H_2O(Pt) + V(Pt)$	2.457E+20	0	0.00
		7.756E+25	0.6230	160.00
(S15)*	$H(Pt) + O(Pt) = OH(Pt) + V(Pt)$	2.348E+21	0	0.00
		3.379E+11	0	21.03
(S16)	$NH_3(Pt) + V(Pt) = NH_2(Pt) + H(Pt)$	4.150E+20	0.8602	114.70
		3.995E+28	0	142.89
(S17)*	$NH(Pt) + H(Pt) = NH_2(Pt) + V(Pt)$	9.639E+10	0	9.12
		4.772E+20	0	87.26
(S18)*	$N(Pt) + H(Pt) = NH(Pt) + V(Pt)$	9.604E+22	0	89.08
		4.234E+17	0	74.89
(S19)	$NH_3(Pt) + O(Pt) = NH_2(Pt) + OH(Pt)$	4.099E+23	0	83.26
		5.679E+21	–0.8602	132.47
(S20)	$NO(Pt) + H(Pt) = N(Pt) + OH(Pt)$	1.018E+12	0	22.43
		1.885E+08	0	133.03
(S21)	$N_2O(Pt) + H(Pt) = N_2 + OH(Pt) + V(Pt)$	3.581E+28	0	105.34
		6.523E+16	0.6574	269.64
(S22)	$2NO(Pt) = N_2O(Pt) + O(Pt)$	7.639E+20	0	85.76
		1.299E+30	–0.6092	155.71
(S23)	$NO_2(Pt) + CO(Pt) = NO(Pt) + CO_2 + V(Pt)$	4.366E+21	0	92.77
		2.833E+26	–0.2643	287.66
(S24)	$H_2O(Pt) + CO(Pt) = 2H(Pt) + CO_2$	1.827E+19	0	113.42
		1.941E+32	–1.1104	153.75
(S25)*	$N(Pt) + CO = NCO(Pt)$	1.008E+19	0	101.46
		7.933E+13	0	118.75
(S26)	$NCO(Pt) + H_2O(Pt) = NH_2(Pt) + CO_2 + V(Pt)$	6.237E+21	0	106.32
		7.392E+36	–1.1104	193.31
(S27)*	$N_2O + V(Pt) = N_2O(Pt)$	3.612E+10	0	29.44
		2.046E+11	0	29.44

Reactions on NO_x storage (BaO) sites:

(S28)*	$CO_2 + BaO = BaCO_3$	2.761E+07	0	18.88
		1.307E+03	0	37.64
(S29)*	$NO_2 + BaO = BaO–NO_2$	1.164E+08	0	0.00
		1.292E+01	0	28.55
(S30)	$BaO + NO_2 = BaO–O + NO$	5.249E+07	0	1.97
		2.375E+10	0.2231	16.18
(S31)*	$NO_2 + BaO–NO_2 = NO + BaO–NO_3$	1.978E+08	0	0.00
		1.884E+12	0	35.71
(S32)*	$NO_2 + BaO–NO_3 = Ba(NO_3)_2$	5.740E+07	0	7.29
		4.313E–01	0	22.18

Pt-BaO spillover reactions:

(S33)*	$BaO + O(Pt) = BaO–O + V(Pt)$	3.577E+13	0	74.88
		1.066E+16	0	83.88
(S34)	$BaO–NO_2 + O(Pt) = BaO–NO_3 + V(Pt)$	2.526E+04	0	0.00
		1.585E+08	–0.2231	30.50
(S35)	$BaO–NO_2 + H(Pt) = BaO + NO + OH(Pt)$	4.773E+08	0	2.31
		9.401E+05	0.2231	0.00
(S36)	$Ba(NO_3)_2 + H(Pt) = BaO–NO_2 + NO_2 + OH(Pt)$	7.627E+10	0	42.01
		2.328E+05	0.2231	17.65
(S37)	$BaO–NO_2 + CO(Pt) = BaO–O + N(Pt) + CO_2$	1.692E+12	0	53.99
		7.320E+35	–0.2643	396.44
(S38)	$BaO–NO_3 + CO(Pt) = BaO–NO_2 + CO_2 + V(Pt)$	3.895E+07	0	0.48
		2.997E+12	–0.2643	191.34
(S39)	$Ba(NO_3)_2 + CO(Pt) = BaO–NO_2 + NO_2 + CO_2 + V(Pt)$	2.329E+09	0	39.14
		2.384E+22	–0.2643	215.11
(S40)	$BaO–NO_2 + N(Pt) = BaO–O + N_2O(Pt)$	1.967E+11	0	55.14
		1.810E+23	–0.3861	67.04
(S41)	$BaO–NO_2 + N(Pt) = BaO–O + N_2 + O(Pt)$	1.282E+15	0	98.45
		1.493E+25	0.2713	253.62

(S42)	$BaO–NO_3 + N(Pt) = BaO–O + N_2 + O_2 + V(Pt)$	3.476E+16	0	101.20
		1.488E+18	0.4944	101.45
(S43)	$Ba(NO_3)_2 + N(Pt) = BaO–NO_3 + N_2 + O_2 + V(Pt)$	5.984E+21	0	161.02
		7.962E+25	0.2713	196.43

$Pt\text{-}Ce_2O_3$ spillover reactions:

(S44)*	$O(Pt) + Ce_2O_3 = V(Pt) + Ce_2O_4$	3.329E+07	0	9.87
		3.919E+07	0	27.79
(S45)	$NO(Pt) + NH_3(Pt) + Ce_2O_4 =$	4.190E+35	0	140.00
	$N_2 + H_2O(Pt) + OH(Pt) + Ce_2O_3$	1.718E+26	–0.1890	412.02

Table 2. Relations between the non-core and core reactions.

(S8) = (G3) – (S3) – 0.5*(S6)

(S9) = –2*(G1) – 2*(S1) + (S6) – 2*(S12)

(S10) = –2*(G1) + (G5) – 2*(S1) + 0.5*(S6) – (S12) – (S18) + (S27)

(S11) = –2*(G1) + (G5) – 2*(S1) + 0.5*(S6) – 2*(S12) + (S27)

(S13) = –(G1) + (G2) – (S1) + (S2) – 0.5*(S6)

(S14) = (G4) – (S4) – 0.5*(S6) – (S7) – (S15)

(S16) = (G1) – (G6) + (S1) – (S5) – 0.5*(S6) + 1.5*(S7) + (S12) + (S17) + (S18)

(S19) = (G1) – (G6) + (S1) – (S5) – 0.5*(S6) + 1.5*(S7) + (S12) + (S15) + (S17) + (S18)

(S20) = (S12) + (S15)

(S21) = –(G5) + 0.5*(S6) + (S15) – (S27)

(S22) = –2*(G1) + (G5) – 2*(S1) + 0.5*(S6) + (S27)

(S23) = (G1) – (G2) + (G3) + (S1) – (S2) – (S3)

(S24) = (G3) – (G4) – (S3) + (S4) + (S7)

(S26) = (G3) – (G4) + (S4) + (S7) + (S17) + (S18) – (S25)

(S30) = (G1) – (G2) + 0.5*(S6) + (S33)

(S34) = –(G1) + (G2) – 0.5*(S6) + (S31)

(S35) = (G1) – (G2) + 0.5*(S6) + (S15) – (S29)

(S36) = (G1) – (G2) + 0.5*(S6) + (S15) – (S31) – (S32)

(S37) = (G1) – (G2) + (G3) + (S1) – (S3) + (S12) – (S29) + (S33)

(S38) = (G1) – (G2) + (G3) – (S3) – (S31)

(S39) = (G1) – (G2) + (G3) – (S3) – (S31) – (S32)

(S40) = –(G1) – (G2) + (G5) – (S1) + (S6) – (S12) + (S27) – (S29) + (S33)

(S41) = –(G1) – (G2) – (S1) + 1.5*(S6) – (S12) – (S29) + (S33)

(S42) = –2*(G2) – (S1) + (S6) – (S12) – (S29) – (S31) + (S33)

(S43) = –(G1) – (G2) – (S1) + 0.5*(S6) – (S12) – (S32)

(S45) = –(G1) + (G4) – (G6) – (S1) – (S4) – (S5) + 0.5*(S7) + (S15) – (S44)

Table 3. Gas-phase reactions used in formulating the thermodynamic constraints.

No.	Reaction	K_0 (cgs units)	n	Q (kJ/mol)
(G1)	$\frac{1}{2}N_2 + \frac{1}{2}O_2 = NO$	3.804E+00	0.0241	90.26
(G2)	$\frac{1}{2}N_2 + O_2 = NO_2$	2.774E–02	0.2472	33.26
(G3)	$CO + \frac{1}{2}O_2 = CO_2$	2.474E–04	0.4874	–283.57
(G4)	$H_2 + \frac{1}{2}O_2 = H_2O$	7.817E+01	–0.623	–239.13
(G5)	$N_2 + \frac{1}{2}O_2 = N_2O$	3.443E–04	0.6574	81.06
(G6)	$\frac{1}{2}N_2 + \frac{3}{2}H_2 = NH_3$	9.381E+01	–0.8361	–42.12

6. RESULTS AND DISCUSSION

Simulations of the 21 steady-flow temperature sweep experiments were the main focus of our previous paper [28], so they will not be discussed in detail here. However, because the simulations in this study were carried out with a fully transient code and with a mechanism that includes NO_x and oxygen storage, it is worthwhile to examine a few cases. (Graphical results for the cases not discussed here are given in the Appendix.) Figure 1 compares the computed and observed outlet gas compositions for the case in which the inlet flow contained 500 ppm NO_2 and 1750 ppm CO. Clearly, the agreement is quite good, even for the minor species N_2O, although there are some discrepancies at the lowest temperatures. Figure 2 presents an additional kind of comparison for the case in which 500 ppm NO_2 was fed along with 5000 ppm H_2. Part (a) is for a simulation using the transient reactor code and the full mechanism, while (b) was generated by using the old steady-state code together with a mechanism obtained by deleting all of the storage and spillover reactions but leaving the kinetic parameters of the remaining (Pt) reactions intact. (It should be mentioned that the steady-state code neglects boundary layer mass transfer, although this has little effect.) Comparisons like this led to the decision to re-evaluate the Pt-phase kinetics reported previously rather than leaving them intact, as originally planned. While the two sets of results are in rough qualitative agreement, the simplified approach fails to capture the low-temperature chemistry and shifts the NO_2/NH_3 crossover point by about 56°C. This implies that storage effects were not completely negligible during the temperature sweeps, so it would have been inconsistent to use the old Pt kinetics when evaluating the parameters for the storage reactions. Additional evidence that storage was important can be obtained by comparing the two simulations with the experimental data in part (c). Clearly, only the complete simulation is able to account for the fact that the outlet NH_3 concentration overshoots the inlet NO_x concentration of 500 ppm. The release of stored NO_x is the only reasonable explanation for this overshoot.

Turning to the simulations of the long storage/regeneration cycles, Figure 3 shows the computed and experimental outlet gas compositions for the cycle carried out at a nominal temperature of 200°C. The simulation shows an unwanted spike of NO at the rich-lean transition (just after $t = 0$), but the seriousness of this is uncertain, given that the experimental plot shows anomalous

amounts of CO exiting the channel over the same time period. Aside from this issue, the most significant shortcoming in the simulation is the slip of NO through the catalyst coincident with the peak of NH_3 production during regeneration. This artifact was a persistent feature during the mechanism development process and resisted all attempts to remove it. One possible explanation is that, according to temperature ramp experiments such as that in Figure 1(b), NO and NH_3 can coexist at temperatures well in excess of 200°C. Thus, it may not be possible for the optimization process to reconcile all of the various pieces of experimental data. However, it must be remembered that the residence time in the temperature ramps was a factor of 3.3 shorter than in the cycles, so direct comparisons are problematic. Another possible explanation for the NO peak is simply an uncertainty in the temperature: If the reaction between NO and NH_3 does become rapid just above 200°C, then any excursions around the critical temperature can be expected to have disproportionate effects.

On a more positive note, the N_2O peak that appears at the lean-rich transition (900 s) is simulated quite accurately, as is the appearance time for NH_3. Accounting for the observed N_2O formation was found to be impossible until the spillover reaction (S40) was added to the mechanism, although this may actually cause N_2O to appear somewhat too rapidly.

It should be noted that the abrupt appearance of NO_2 at about 150 s in Figure 3(b) is an illusion brought about by experimental error. Because the NO_2 concentration was actually determined by difference between total NO_x and NO, it was subject to large relative errors when the latter two values were close to each other. For short times, the computed NO_2 concentration was in fact slightly negative, and of course the model is incapable of reproducing this.

Comparison plots for the long cycle run at 300°C are shown in Figure 4. The simulation reproduces all of the important qualitative features of the experiment, although there are modest quantitative inaccuracies: The initial rises of NO and NO_2 during storage are too rapid, there is a small but unwanted spike in N_2O at the lean-rich transition, there is excessive slip of NO during the first part of regeneration, and the NH_3 peak is somewhat too high. It should be noted that the NO slip is unlike that of Figure 3(a), in that it now occurs almost entirely before the breakthrough of NH_3; the reaction between these two species at 300°C is too rapid for them to

coexist to any great extent at the reactor exit. Note also that, even though the peak concentration of NH_3 is overpredicted, the timing of the peak is precisely correct, even though it occurs roughly 100 s later than at 200°C. Furthermore, the integrated amount of NH_3 exiting the channel is simulated quite accurately (as is the case in Figure 3).

Finally, the comparison plots for the cycle at 400°C are in Figure 5. Here the amounts of N_2O and NH_3 being produced are so small as to be of little interest. Still, it is worth noting that the position of the NH_3 peak is well reproduced once again, even though it is slightly earlier than even at 200°C. Regardless of these details, however, the most significant feature of the plots is the large NO puff that immediately follows the switch to rich conditions. The simulation captures the experimental behavior quite well. The simple appearance of these plots relative to those at 200°C and 300°C suggests that the results are more heavily influenced by equilibrium considerations, with most of the released NO_x being converted to the very stable but unseen N_2 rather than the less- and more-heavily reduced forms N_2O and NH_3. Some confirmation of this lies in the fact that the equilibrium between NO and NO_2 in 10% O_2 at 1 atm and 407°C (the actual temperature during the latter part of the storage phase) is almost precisely a 50/50 mixture. The fact that the simulation and the experimental data differ somewhat from this and from each other may be due to measurement errors, uncertainty in the actual values of the temperature and pressure, or failure to achieve equilibrium after all.

Although not confirmed by direct observation, Figure 6 shows two examples of the time evolution of the surface composition predicted by the reactor model. Specifically, this shows the spatially-averaged site fractions of the various species on the BaO phase during the 200°C and 300°C cycles. The two plots are similar, so we will focus attention on the latter for concreteness. Because regeneration of the catalyst is complete at 300°C, the cycle starts with a surface that is a mixture of carbonate and bare oxide, with relative amounts specific to this temperature. After the inflow of NO and O_2 begins, BaO–O and BaO–NO_2 begin to appear on the surface immediately, while there are apparent lags for BaO–NO_3 and $Ba(NO_3)_2$. As will be shown later, most of the BaO–O production is probably due to the spillover reaction (S33). However, it is clear that this species is highly reactive, as the rise in its concentration is quickly halted and a slow decline begins. The consumption of BaO–O is undoubtedly due to (S30) operating in

reverse, given the large concentration of available NO. At the same time, NO_2 produced via either (S30) or the oxidation of NO on Pt sites can react with BaO via (S29) to produce BaO–NO_2. The consumption of BaO by (S33) and (S29) forces (S28) to the left, thereby decomposing the carbonate. Eventually NO_2 and BaO–NO_2 are present in sufficient quantities to give BaO–NO_3 via (S31). However, the simulation results show that the latter species is also fairly reactive, as its concentration reaches a long but low plateau. The obvious avenue for its consumption is (S32), and the combination of (S31) and (S32) causes the concentration of BaO–NO_2 to fall as that of $Ba(NO_3)_2$ rises, as shown in the figure. Under oxidizing conditions, there is no route for the decomposition of $Ba(NO_3)_2$, so it continues to accumulate until the lean-rich transition.

Because all of the reactions are written as reversible, the proposed sequence of events could in theory be reversed during the regeneration part of the cycle. However, the spillover reactions (S35)–(S43) provide a more assertive path for the reduction and/or decomposition of the three stored NO_x species under reducing conditions. In fact, the existence of such reactions appears to be necessary to produce a sharp reaction front during regeneration. Another consequence, as seen in Figure 6(b), is that all three stored NO_x species can be consumed simultaneously, in contrast with the BaO–NO_2 vs. $Ba(NO_3)_2$ tradeoff that is seen during storage. The small rise in BaO–NO_3 that occurs just after 900 s must be due to either (S32), operating in reverse with NO_2 suddenly absent, or (S43), which uses the same N(Pt) species that gives rise to a spike in N_2O via (S40) at the same time. In any case, at the end of the cycle, the surface is free of stored NO_x and the composition is exactly as it was at the start, in accordance with the periodicity requirement.

The simulations can also be used to examine the spatial progression of the gas composition down the monolith channel, and in particular to see whether the model is consistent with conjectures about the role of NH_3 as a reduction intermediate [13]. Figure 7 shows axial profiles of the gas concentrations at two distinct times (950 s and 1050 s) during the regeneration of the catalyst at 300°C. As seen in Figure 4, at both of these moments the regeneration is well underway, with some NO, NO_2, and N_2O slipping through the catalyst, but with NH_3 not yet appearing at the exit. However, Figure 7 shows that NH_3 is certainly involved in the chemistry within the channel. At 950 s not even the upstream end of the channel is completely regenerated, and NO_x

released in this region is reduced all the way to NH_3 upon encountering a large excess of primary reductants (CO and H_2). The NH_3 concentration continues to grow until these reductants are nearly exhausted. Beyond that, not only does NH_3 formation cease, but this species itself reacts with the desorbing NO_x (and oxygen) and is thus rapidly consumed. The disappearance of NH_3 marks the end of reducing conditions, so NO_x, N_2O, and oxygen released or produced downstream of that point simply accumulate and exit the channel. By 1050 s the first few cm of the channel have been largely (but not completely) cleansed of stored NO_x, so the position of maximum NH_3 production appears further downstream, but the sequence of events is the same. Eventually, of course, NH_3 forms sufficiently far downstream that it survives to the channel exit, and breakthrough is observed. Still later, there is insufficient NO_x remaining on the surface for any NH_3 to be formed, and regeneration is essentially complete.

Obviously, the various reactions in the mechanism do not contribute equally to the simulated LNT behavior, and it is natural to wonder about their relative importance. During the parameter optimization, reactions that were found to be completely noncontributing were deleted from further consideration, so those listed in Table 1 are by definition relevant to at least a small extent. Quantitative information about their relative importance is contained in Table 4. This table was compiled by deleting individual reactions (forward and reverse) one at a time from the mechanism and observing the effect on the fit to the data. Specifically, the table gives the percent increases in the objective functions for the long cycles, the temperature ramps, and the overall data set resulting from the deletion of each reaction. This is not a perfect approach to the question, as some of the reactions have roles that are clearly linked, but the table actually provides clues to such linkages. For example, the entries for reactions (S25) and (S26) are nearly identical, corresponding to the fact that the deletion of either reaction destroys the isocyanate pathway for NH_3 formation. This is further evidenced by the fact that the deletion of both reactions (not shown) has exactly the same effect as the deletion of (S25) alone. Clearly, the temperature ramps are affected much more strongly than are the cycles, implying that the conditions leading to isocyanate formation are not often encountered in the latter. Closer examination confirms that the effect of either reaction on the temperature ramps is confined almost entirely to those experiments in which CO was used as the reductant. Because CO was also used in the cycles (in conjunction with H_2), one would expect the isocyanate route to be

important here as well; the results show that it does indeed make a significant contribution, but only at 200°C. This supports our earlier conclusion [28] that isocyanate formation, unlike the water-gas shift reaction, provides basically a low-temperature pathway to NH_3 formation.

Linkages aside, it is clear that the individual reactions range in importance from marginal to absolutely crucial. The two reactions that are central to the role of H_2O, namely (S4) and especially (S14), are the most influential overall and affect both the ramps and the cycles very strongly. On the other hand, the water-gas shift reaction, (S24), is extremely important in the cycles but less so in the ramps; this differs greatly from what is seen for its competitor, the isocyanate pathway, as noted above. Regardless of the pathway used to make NH_2(Pt), the remaining steps needed to form NH_3, namely (S16) and (S5), are critically important. Obviously, many of the other reactions describing adsorption and recombination chemistry on the Pt sites are also essential. A surprising exception is the CO oxidation reaction (S8), although we have found that the importance of this reaction depends strongly on the fine details of the overall mechanism. Two other surprises are (S13) and (S2), which might be regarded as crucial in oxidizing NO to NO_2 in preparation for storage, but which are actually found to make only small contributions to the cycle simulations. The resolution to this paradox lies in reaction (S33), which is by far the most important of the spillover reactions in determining the cycling behavior. As suggested by the nearly identical sensitivities for (S33) and (S30), O(Pt) is used primarily to oxidize BaO to BaO–O in preparation for reaction with gas-phase NO, as opposed to oxidizing NO that is already adsorbed on a Pt site. Either route is consistent with the experimental observation that NO is not easily stored on a catalyst that lacks a precious metal component, as discussed in the Introduction. However, the BaO–O pathway also explains how NO can be stored at temperatures of 200°C and below, where its oxidation to NO_2 on Pt is very slow. This approach appears to be in sharp contrast with that of Lindholm et al. [17], which allows the direct deposition of NO on both carbonate and so-called S_3 sites. Kabin et al. [45] argued for the importance of the spillover reaction (S33) and suggested that the formation of BaO–O was followed by the attachment of gas-phase NO and/or NO_2, as in (9) and (10) above. While the latter two reactions do not appear explicitly in the current mechanism, they can be formed from simple combinations of (S29)–(S31).

Not surprisingly, the oxygen storage reaction (S44) plays only a minor role in the temperature ramps, as was the intent in the experimental design. However, it is quite important in simulating the cycles, so any mechanism describing a catalyst with an oxygen storage component must include such a reaction.

The sensitivity analysis also sheds light on the production of N_2, which is easy to overlook due to the use of N_2 as the bath gas. Of the possible routes, the simple atom recombination (S9) is clearly crucial, while the neutralization (S45) and the spillover reactions (S41)–(S43) are of lesser importance, especially in the temperature ramps. Interestingly, the remaining route (S21) affects the ramps strongly but the cycles not at all. This is almost certainly due to the fact that two of the ramps involved a feed of N_2O in a large excess of reductant. Evidently this particular combination of reactants did not present itself to a significant degree during the cycle experiments.

As alluded to earlier, the spillover reaction (S45) is something of a special case in the mechanism. Technically, the inclusion of this reaction is very slightly detrimental to the overall data fit, although it does have a noticeable positive effect on the cycle simulations. The overriding reason for retaining this reaction, as noted above, is that it drastically curtails the amount of NH_3 that is produced during more traditional short (60 s/5 s) cycles. In other words, it exists to account for a set of circumstances that is apparently not well represented in our primary experiments. The long cycles have the obvious advantage that they allow for a time-resolved measurement of the effluent gas composition, whereas analyses dealing with short cycles can generally consider only cycle-averaged values. However, there is always a possibility that some phenomena will be different. The rate chosen for (S45) in Table 1 solves the NH_3 production problem without significantly affecting the primary data fit one way or the other.

Finally, we wish to show how the microkinetic mechanism proposed here relates to some key global reactions that have been presented in the literature. One such reaction describes the overall formation of the stoichiometric nitrate from gas-phase NO_2 and unused BaO sites:

$$2NO_2 + (1/2)O_2 + BaO \rightarrow Ba(NO_3)_2 \qquad (13)$$

It is easily verified that the combination (S29) – (S30) + (S31) + (S32) + (S33) + 0.5(S6) reproduces this exactly. Combining these reactions appears to be reasonable, because all of them have large sensitivities in Table 4. Still, there is no guarantee that the individual steps will take place at the rates necessary to produce the overall stoichiometry in Eq. (13). It must also be remembered that the "clean" BaO surface actually contains a substantial amount of $BaCO_3$ in the presence of gas-phase CO_2, so the species on the left of Eq. (13) do not constitute a complete list of reactants.

A second global reaction that has been proposed is the overall disproportionation [46]

$$3NO_2 + BaO \rightarrow NO + Ba(NO_3)_2 \qquad (14)$$

This is equivalent to the combination (S29) + (S31) + (S32).

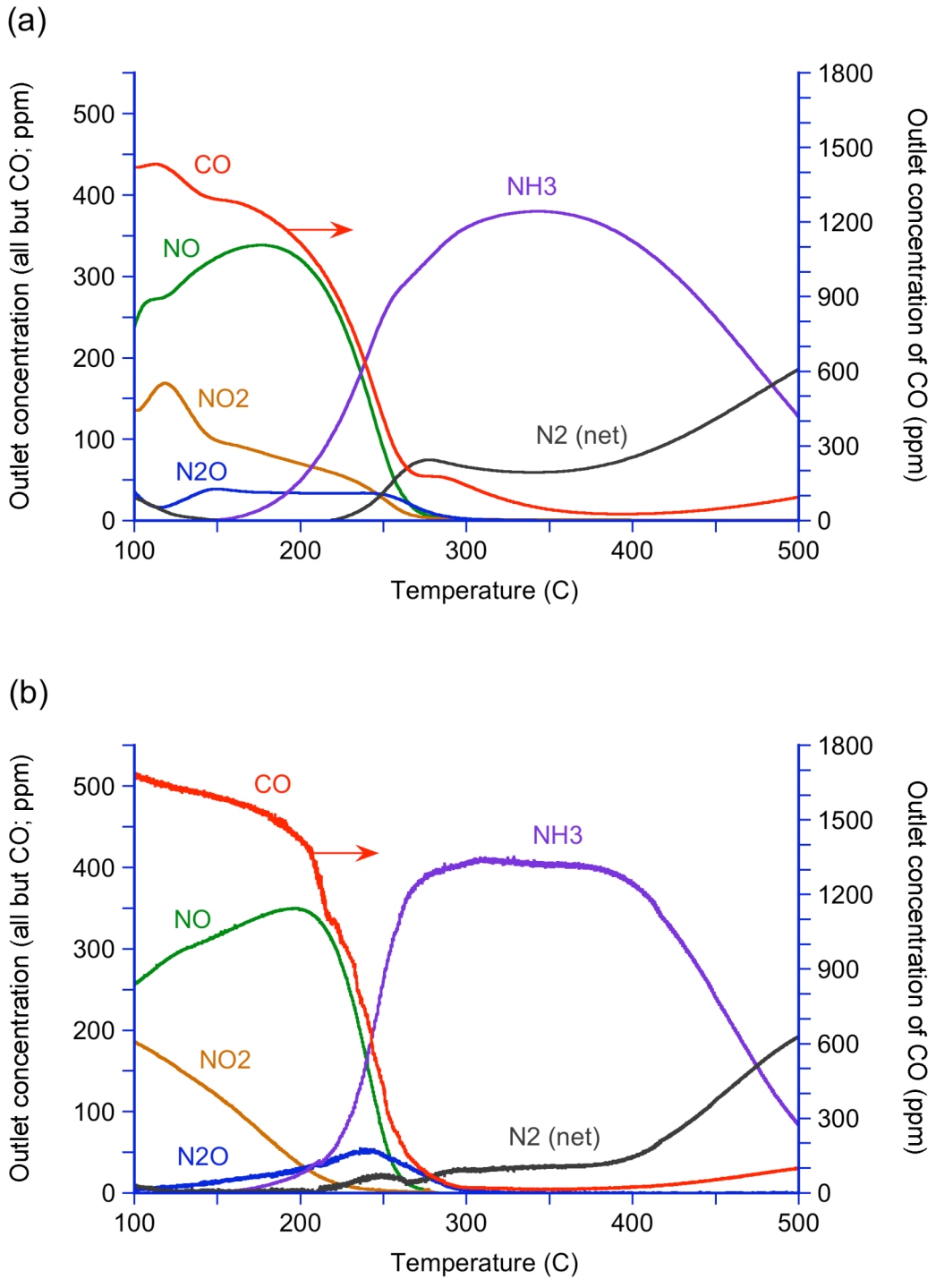

Figure 1. Outlet gas phase concentrations during temperature sweep with an inlet mixture containing 500 ppm NO_2 and 1750 ppm CO (net reducing conditions). (a) simulation results; (b) experimental measurements.

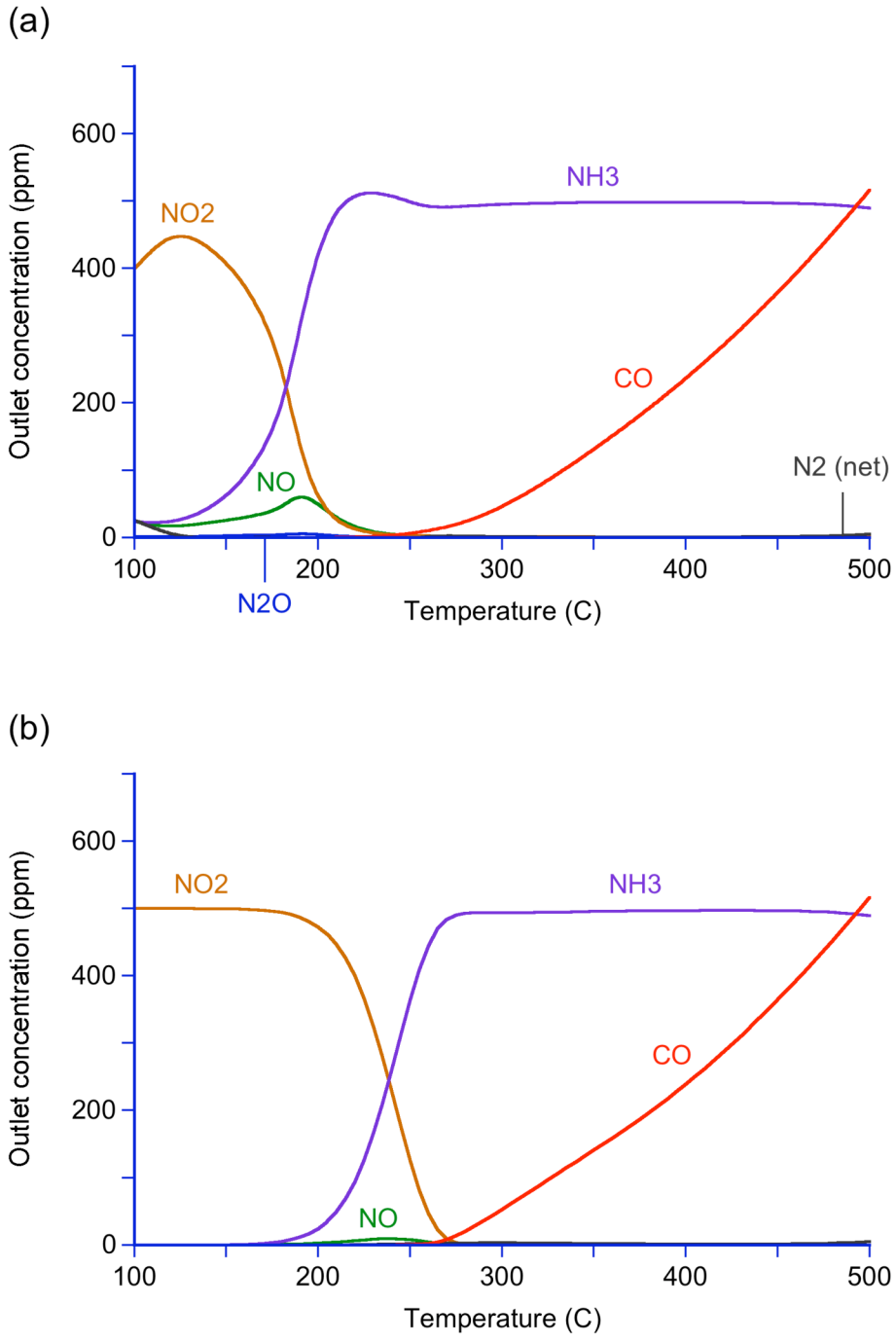

Figure 2. Outlet gas phase concentrations during temperature sweep with an inlet mixture containing 500 ppm NO_2 and 5000 ppm H_2 (strongly reducing conditions). (a) simulation results using transient code and full mechanism; (b) simulation results using steady-state code (with mass transfer neglected) and precious metal mechanism.

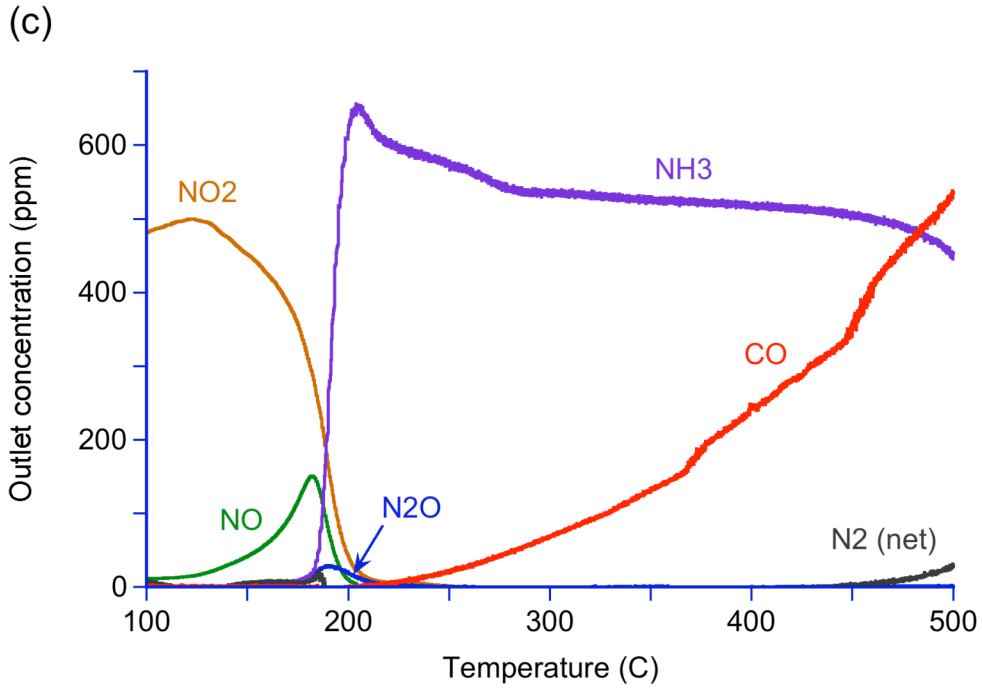

Figure 2 (continued). Outlet gas phase concentrations during temperature sweep with an inlet mixture containing 500 ppm NO_2 and 5000 ppm H_2 (strongly reducing conditions). (c) experimental measurements.

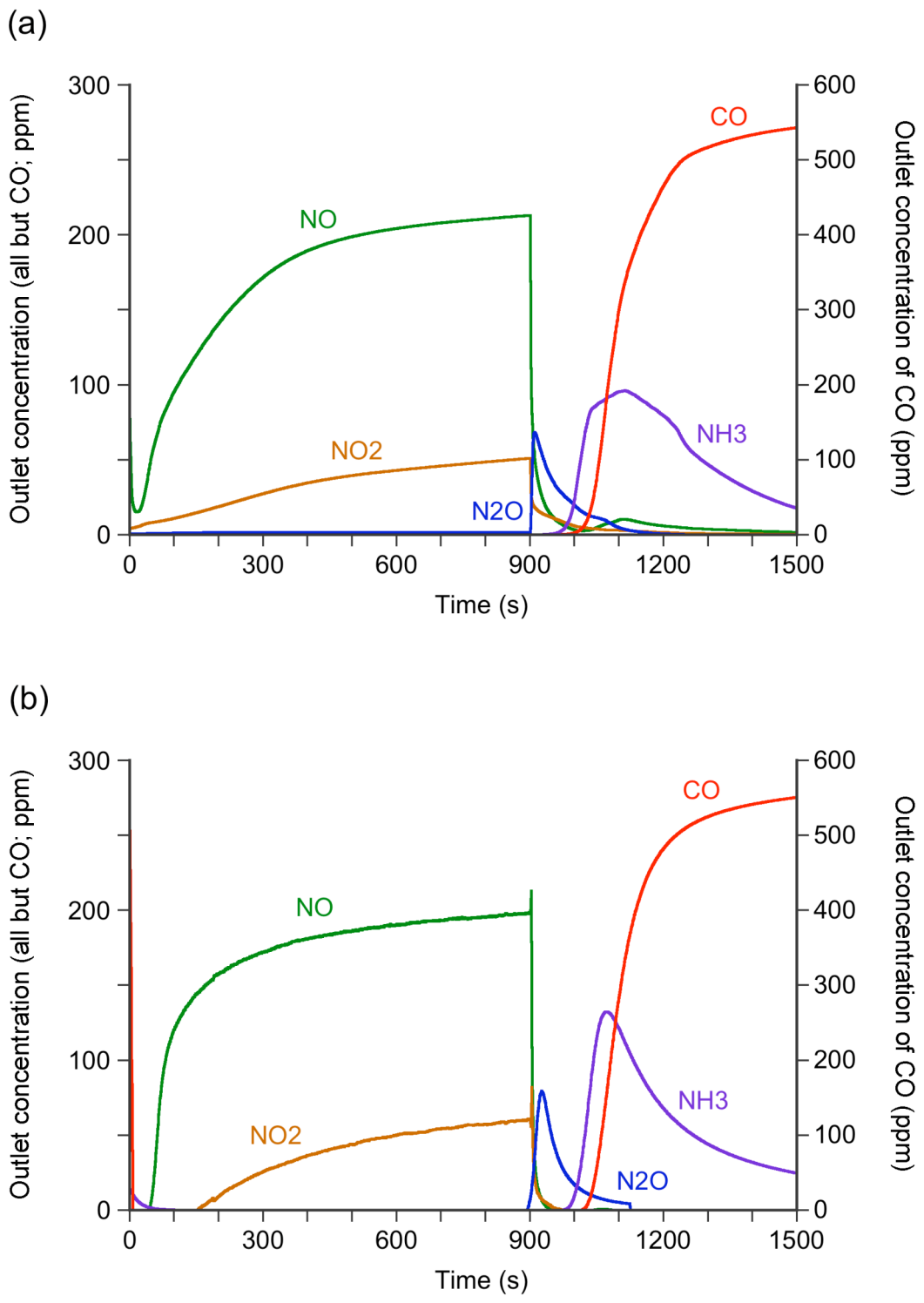

Figure 3. Outlet gas phase concentrations during long storage/regeneration cycle at 200°C. (a) simulation results; (b) experimental measurements.

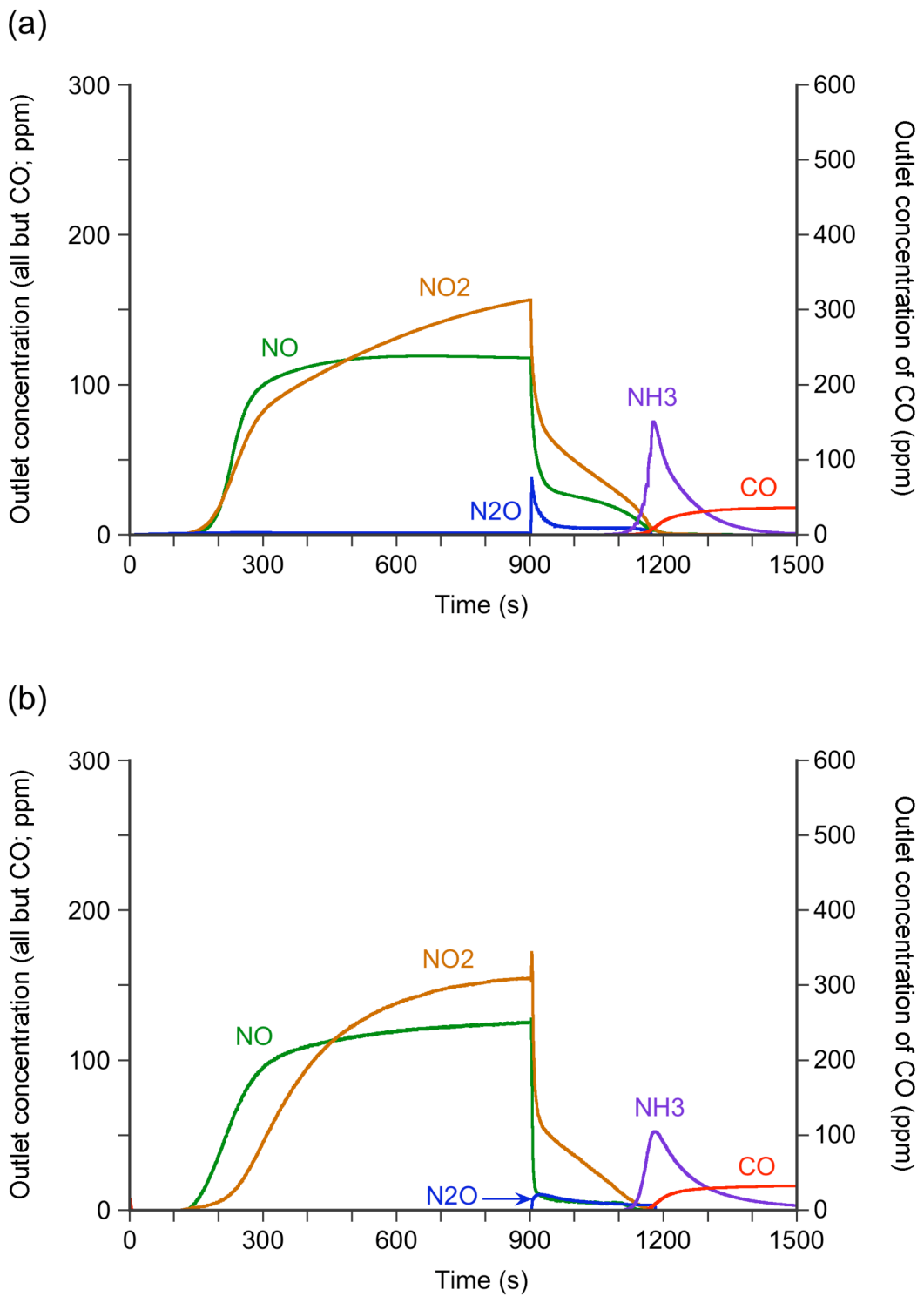

Figure 4. Outlet gas phase concentrations during long storage/regeneration cycle at 300°C. (a) simulation results; (b) experimental measurements.

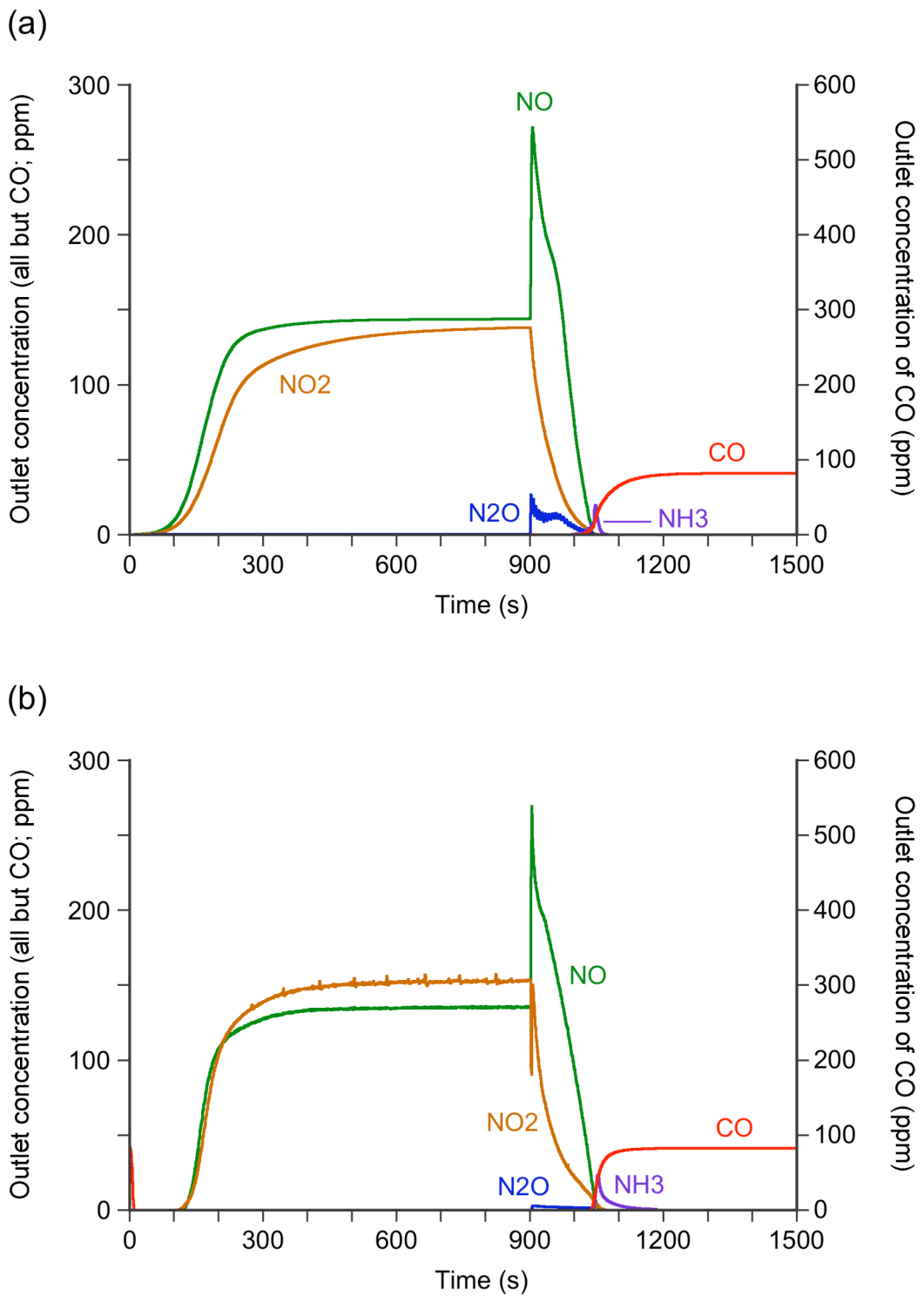

Figure 5. Outlet gas phase concentrations during long storage/regeneration cycle at 400°C. (a) simulation results; (b) experimental measurements.

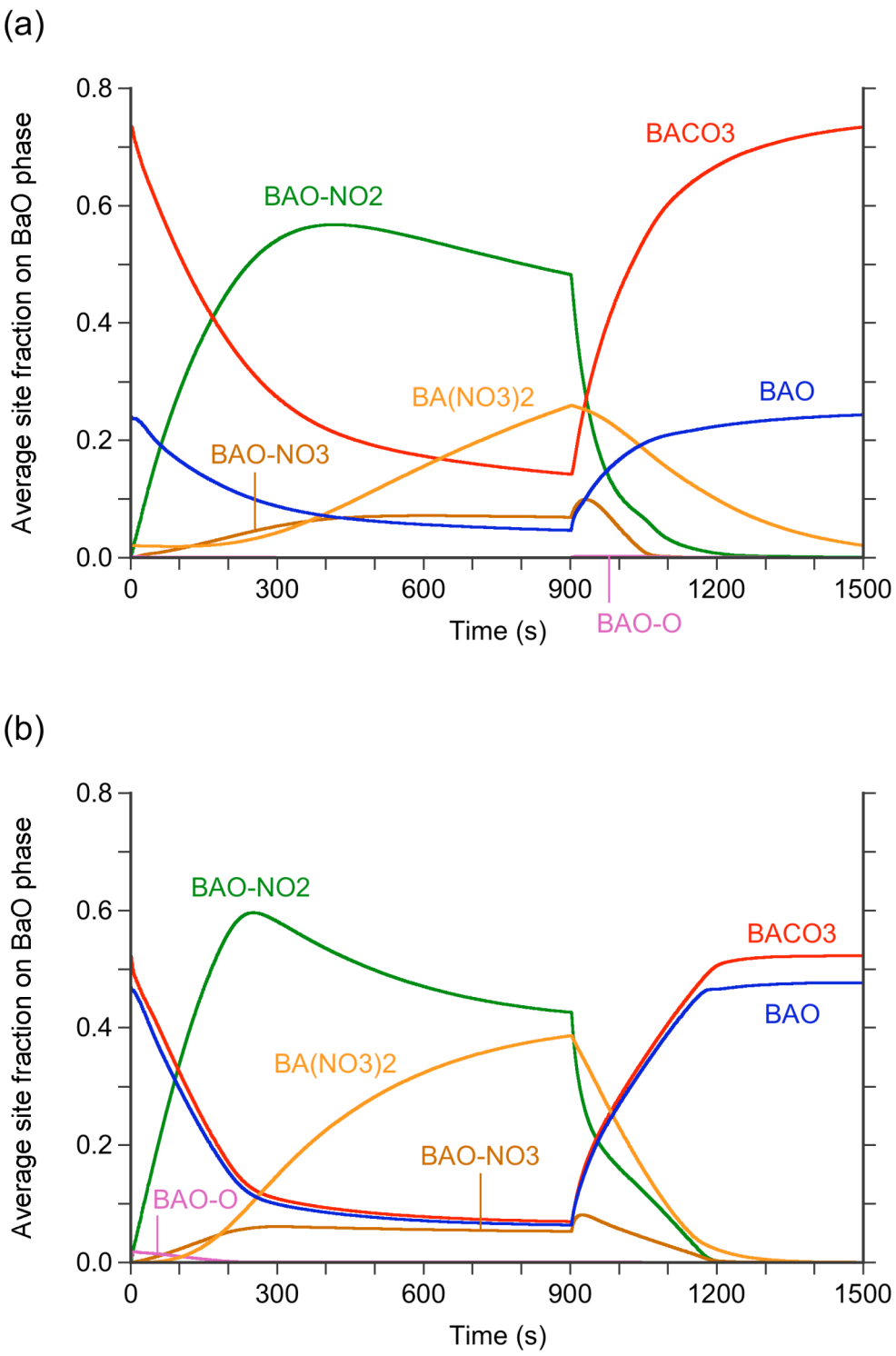

Figure 6. Predicted spatially-averaged site fractions of BaO-phase surface species during long storage/regeneration cycle. (a) 200°C; (b) 300°C.

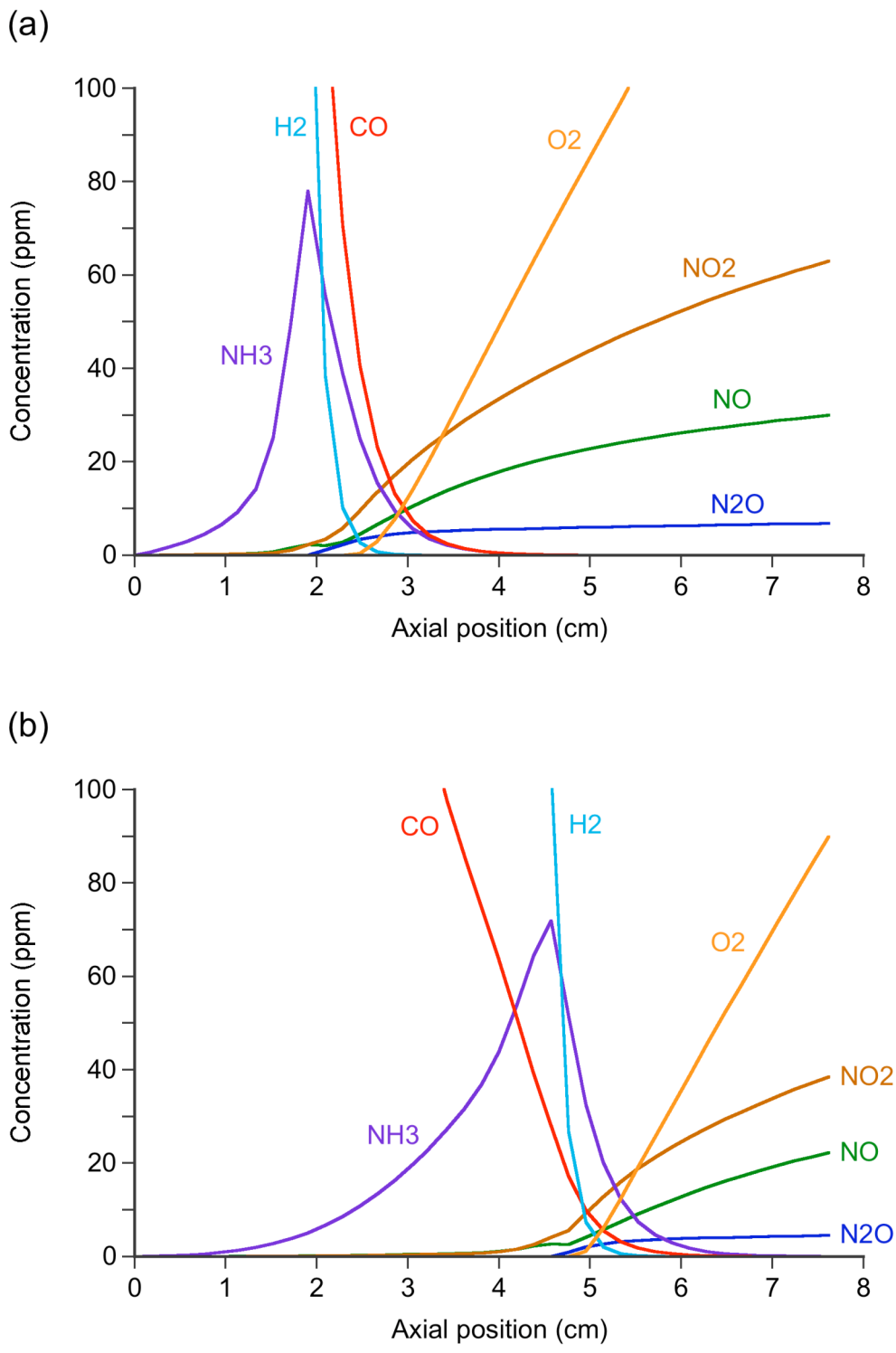

Figure 7. Predicted axial profiles of gas phase concentrations at two distinct times during long storage/regeneration cycle at 300°C. (a) 950 s; (b) 1050 s.

Table 4. Percent increases in the objective functions resulting from the deletion of individual reactions in the mechanism.

Reaction	Cycles	Temperature ramps	Overall
(S1)	85.7	479.9	417.7
(S2)	11.0	31.6	27.2
(S3)	510.5	219.1	303.6
(S4)	523.4	620.3	599.5
(S5)	61.1	530.4	459.8
(S6)	548.1	161.9	284.5
(S7)	393.7	385.4	387.2
(S8)	3.3	12.1	10.1
(S9)	12.0	158.2	133.3
(S10)	0.0	6.3	4.9
(S11)	0.2	4.2	3.3
(S12)	146.1	310.6	279.7
(S13)	10.9	14.6	13.8
(S14)	825.1	765.7	779.3
(S15)	352.9	89.6	172.2
(S16)	202.8	448.8	403.8
(S17)	85.6	388.4	338.6
(S18)	110.8	586.5	512.2
(S19)	28.6	169.9	145.2
(S20)	0.0	2.5	1.9
(S21)	0.0	73.6	60.0
(S22)	0.3	46.0	37.0
(S23)	0.1	18.7	14.8
(S24)	484.5	96.6	227.1
(S25)	7.0	121.4	101.3
(S26)	6.9	121.3	101.2

(S27)	7.1	87.6	72.7
(S28)	250.3	59.0	117.3
(S29)	758.1	36.1	324.8
(S30)	535.9	14.2	218.3
(S31)	151.8	163.9	161.1
(S32)	150.4	81.8	99.3
(S33)	536.0	13.6	218.2
(S34)	43.9	0.0	11.4
(S35)	6.6	17.8	15.3
(S36)	1.0	33.2	26.6
(S37)	6.5	2.5	3.4
(S38)	10.1	18.9	16.9
(S39)	9.9	1.0	3.0
(S40)	4.9	1.1	1.9
(S41)	3.1	0.0	0.7
(S42)	2.2	1.7	1.8
(S43)	16.8	1.7	5.3
(S44)	88.4	5.4	28.8
(S45)	2.8	–1.1	–0.3

7. CONCLUSIONS

We have developed a thermodynamically consistent microkinetic surface reaction mechanism that accounts quite well for the behavior of a fully formulated lean NO_x trap under a wide variety of conditions. Successful simulations of the reacting flow in a monolith channel have been carried out with a transient plug flow code that includes mass transfer resistances in the gas phase boundary layer but not the washcoat. The mechanism has some difficulty in predicting the amounts of N_2O and NH_3 formed during long storage/regeneration cycles at some temperatures, just as was true for the steady flow temperature sweep experiments considered earlier [28]. The cycle simulations make some interesting predictions about the details of the chemistry taking place during both storage and regeneration. In particular, the oxidation of BaO by spillover from adjacent precious metal sites is found to be more important than oxidation of adsorbed NO to NO_2. In accordance with general belief, NH_3 is found to be a ubiquitous intermediate during the reduction of released NO_x by a CO/H_2 mixture. As inferred earlier, the isocyanate pathway for NH_3 formation, which can be crucial to explaining experiments in which CO is used as a reductant, seems to be operative only at relatively low temperatures. In any case, the mechanism presented here seems to give a good representation of the overall chemistry, and it should be useful as a starting point in similar investigations of catalyst sulfation/desulfation and regeneration in the presence of alternative reductants.

REFERENCES

1. Bevan, K.E., Taylor, W., 2006. Simulated performance of a diesel aftertreatment system for U.S. 2010 application. SAE paper 2006-01-3551.

2. Hu, H., Reuter, J., Yan, J., McCarthy, J., 2006. Advanced NO_x aftertreatment system and controls for on-highway heavy duty diesel engines. SAE paper 2006-01-3552.

3. Theis, J.R., Gulari, E., 2006. A LNT+SCR system for treating the NO_x emissions from a diesel engine. SAE paper 2006-01-0210.

4. Parks, J.E., Prikhodko, V.Y., 2009. Ammonia production and utilization in a hybrid LNT+SCR system. SAE paper 2009-01-2739.

5. Larsson, M., Andersson, L., Fast, O., Litorell, M., Makuie, R., 1999. NO_x trap control by physically based model. SAE paper 1999-01-3503.

6. Ketfi-Cherif, A., von Wissel, D., Beurthey, S., Sorine, M., 2000. Modeling and control of a NO_x trap catalyst. SAE paper 2000-01-1199.

7. Kim, Y.-W., Sun, J., Kolmanovsky, I., Koncsol, J., 2003. A phenomenological control oriented lean NO_x trap model. SAE paper 2003-01-1164.

8. Laurent, F., Pope, C.J., Mahzoul, H., Delfosse, L., Gilot, P., 2003. Modelling of NO_x adsorption over NO_x adsorbers. Chemical Engineering Science 58, 1793–1803.

9. Koci, P., Marek, M., Kubicek, M., Maunula, T., Harkonen, M., 2004. Modelling of catalytic monolith converters with low- and high-temperature NO_x storage compounds and differentiated washcoat. Chemical Engineering Journal 97, 131–139.

10. Olsson, L., Blint, R.J., Fridell, E., 2005. Global kinetic model for lean NO_x traps. Industrial & Engineering Chemistry Research 44, 3021–3032.

11. Guthenke, A., Chatterjee, D., Weibel, M., Waldbusser, N., Koci, P., Marek, M., Kubicek, M., 2007. Development and application of a model for a NO_x storage and reduction catalyst. Chemical Engineering Science 62, 5357–5363.

12. Koop, J., Deutschmann, O., 2007. Modeling and simulation of NO_x abatement with storage/reduction catalysts for lean burn and diesel engines. SAE paper 2007-01-1142.

13. Bhatia, D., Clayton, R.D., Harold, M.P., Balakotaiah, V., 2009. A global kinetic model for NO_x storage and reduction on $Pt/BaO/Al_2O_3$ monolithic catalysts. Catalysis Today 147, S250–S256.

14. Koci, P., Plat, F., Stepanek, J., Bartova, S., Marek, M., Kubicek, M., Schmeisser, V., Chatterjee, D., Weibel, M., 2009. Global kinetic model for the regeneration of NO_x storage catalyst with CO, H_2 and C_3H_6 in the presence of CO_2 and H_2O. Catalysis Today 147, S257–S264.

15. Olsson, L., Persson, H., Fridell, E., Skoglundh, M., Andersson, B., 2001. Kinetic study of NO oxidation and NO_x storage on Pt/Al_2O_3 and $Pt/BaO/Al_2O_3$. Journal of Physical Chemistry B 105, 6895–6906.

16. Olsson, L., Fridell, E., Skoglundh, M., Andersson, B., 2002. Mean field modelling of NO_x storage on $Pt/BaO/Al_2O_3$. Catalysis Today 73, 263–270.

17. Lindholm, A., Currier, N.W., Li, J., Yezerets, A., Olsson, L., 2008. Detailed kinetic modeling of NO_x storage and reduction with hydrogen as the reducing agent and in the presence of CO_2 and H_2O over a Pt/Ba/Al catalyst. Journal of Catalysis 258, 273–288.

18. Xu, J., Clayton, R., Balakotaiah, V., Harold, M.P., 2008. Experimental and microkinetic modeling of steady-state NO reduction by H_2 on $Pt/BaO/Al_2O_3$ monolith catalysts. Applied Catalysis B: Environmental 77, 395–408.

19. Roy, S., Baiker, A., 2009. NO_x storage-reduction catalysis: From mechanism and materials properties to storage-reduction performance. Chemical Reviews 109, 4054–4091.

20. Scotti, A., Nova, I., Tronconi, E., Castoldi, L., Lietti, L., Forzatti, P., 2004. Kinetic study of lean NO_x storage over the $Pt\text{-}Ba/Al_2O_3$ system. Industrial & Engineering Chemistry Research 43, 4522–4534.

21. Prinetto, F., Ghiotti, G., Nova, I., Lietti, L., Tronconi, E., Forzatti, P., 2001. FT-IR and TPD investigation of the NO_x storage properties of BaO/Al_2O_3 and $Pt\text{-}BaO/Al_2O_3$ catalysts. Journal of Physical Chemistry B 105, 12732–12745.

22. Prinetto, F., Ghiotti, G., Nova, I., Castoldi, L., Lietti, L., Tronconi, E., Forzatti, P., 2003. In situ FT-IR and reactivity study of NO_x storage over $Pt\text{-}Ba/Al_2O_3$ catalysts. Physical Chemistry Chemical Physics 5, 4428–4434.

23. Nova, I., Castoldi, L., Lietti, L., Tronconi, E., Forzatti, P., Prinetto, F., Ghiotti, G., 2004. NO_x adsorption study over Pt-Ba/alumina catalysts: FT-IR and pulse experiments. Journal of Catalysis 222, 377–388.

24. Elizundia, U., Lopez-Fonseca, R., Landa, I., Gutierrez-Ortiz, M.A., Gonzalez-Velasco, J.R., 2007. FT-IR study of NO_x storage mechanism over $Pt/BaO/Al_2O_3$ catalysts. Effect of the Pt-BaO interaction. Topics in Catalysis 42-43, 37–41.

25. Hess, C., Lunsford, J.H., 2002. Mechanism for NO_2 storage in barium oxide supported on magnesium oxide studied by in situ Raman spectroscopy. Journal of Physical Chemistry B 106, 6358–6360.

26. Hess, C., Lunsford, J.H., 2003. NO_2 storage and reduction in barium oxide supported on magnesium oxide studied by in situ Raman spectroscopy. Journal of Physical Chemistry B 107, 1982–1987.

27. Dumesic, J.A., 1999. Analyses of reaction schemes using De Donder relations. Journal of Catalysis 185, 496–505.

28. Larson, R.S., Pihl, J.A., Chakravarthy, V.K., Toops, T.J., Daw, C.S., 2008. Microkinetic modeling of lean NO_x trap chemistry under reducing conditions. Catalysis Today 136, 104–120.

29. Pihl, J.A., Parks, J.E., Daw, C.S., Root, T.W., 2006. Product selectivity during regeneration of lean NO_x trap catalysts. SAE paper 2006-01-3441.

30. Griffin, J.D., Kolda, T.G., Lewis, R.M., 2006. Asynchronous parallel generating set search for linearly-constrained optimization. Sandia National Laboratories Report SAND2006-4621.

31. Kee, R.J., Rupley, F.M., Miller, J.A., Coltrin, M.E., Grcar, J.F., Meeks, E., Moffat, H.K., Lutz, A.E., Dixon-Lewis, G., Smooke, M.D., Warnatz, J., Evans, G.H., Larson, R.S., Mitchell, R.E., Petzold, L.R., Reynolds, W.C., Caracotsios, M., Stewart, W.E., Glarborg, P., 1999. CHEMKIN Collection, Release 3.5, Reaction Design, Inc., San Diego, CA.

32. Caracotsios, M., Stewart, W.E., 1985. Sensitivity analysis of initial-value problems with mixed ODEs and algebraic equations. Computers & Chemical Engineering 9, 359–365.

33. Tronconi, E., Forzatti, P., 1992. Adequacy of lumped parameter models for SCR reactors with monolith structure. AIChE Journal 38, 201–210.

34. Pihl, J.A., 2005. Byproduct formation during regeneration of lean NO_x traps. M.S. Thesis, University of Wisconsin–Madison.

35. Sedlmair, C., Seshan, K., Jentys, A., Lercher, J.A., 2003. Elementary steps of NO_x adsorption and surface reaction on a commercial storage-reduction catalyst. Journal of Catalysis 214, 308–316.

36. Balcon, S., Potvin, C., Salin, L., Tempere, J.F., Djega-Mariadassou, G., 1999. Influence of CO_2 on storage and release of NO_x on barium-containing catalyst. Catalysis Letters 60, 39–43.

37. Machida, M., Kurogi, D., Kijima, T., 2003. Role of hydrogen-spillover in H_2-NO reaction over Pd-supported NO_x-adsorbing material, MnO_x-CeO_2. Journal of Physical Chemistry B 107, 196–202.

38. Su, Y., Amiridis, M.D., 2004. In situ FTIR studies of the mechanisim of NO_x storage and reduction on Pt/Ba/Al_2O_3 catalysts. Catalysis Today 96, 31–41.

39. Takahashi, N., Yamazaki, K., Sobukawa, H., Shinjoh, H., 2007. The low-temperature performance of NO_x storage and reduction catalyst. Applied Catalysis B: Environmental 70, 198–204.

40. Mulla, S.S., Chen, N., Cumaranatunge, L., Delgass, W.N., Epling, W.S., Ribeiro, F.H., 2006. Effect of potassium and water vapor on the catalytic reaction of nitric oxide and dioxygen over platinum. Catalysis Today 114, 57–63.

41. Duprez, D., Descorme, C., Birchem, T., Rohart, E., 2001. Oxygen storage and mobility on model three-way catalysts. Topics in Catalysis 16-17, 49–56.

42. Choi, J.-S., Partridge, W.P., Daw, C.S., 2007. Sulfur impact on NO_x storage, oxygen storage, and ammonia breakthrough during cyclic lean/rich operation of a commercial lean NO_x trap. Applied Catalysis B: Environmental 77, 145–156.

43. Galdikas, A., Descorme, C., Duprez, D., Dong, F., Shinjoh, H., 2004. Study of the oxygen diffusion on three-way catalysts: a kinetic model. Topics in Catalysis 30-31, 405–409.

44. Holmgren, A., Duprez, D., Andersson, B., 1999. A model of oxygen transport in Pt/ceria catalysts from isotope exchange. Journal of Catalysis 182, 441–448.

45. Kabin, K.S., Khanna, P., Muncrief, R.L., Medhekar, V., Harold, M.P., 2006. Monolith and TAP reactor studies of NO_x storage on $Pt/BaO/Al_2O_3$: Elucidating the mechanistic pathways and roles of Pt. Catalysis Today 114, 72–85.

46. Epling, W.S., Parks, J.E., Campbell, G.C., Yezerets, A., Currier, N.W., Campbell, L.E., 2004. Further evidence of multiple NO_x sorption sites on NO_x storage/reduction catalysts. Catalysis Today 96, 21–30.

APPENDIX

On the following pages are shown the simulated and measured outlet gas concentrations for 19 of the 21 steady flow temperature sweep experiments described in [28], specifically, all of the experiments not discussed above in Section 6.

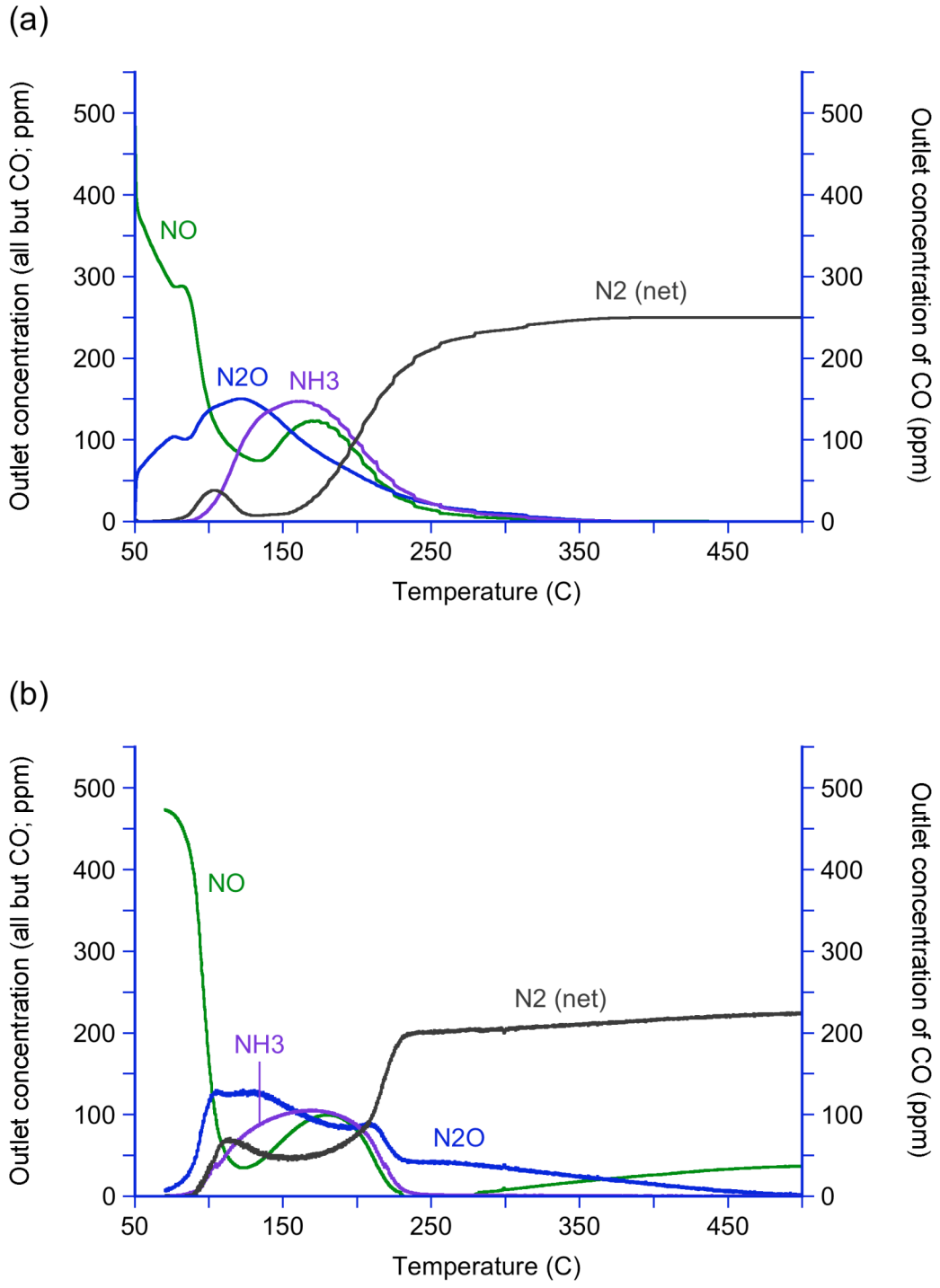

Figure A1. Outlet gas phase concentrations during temperature sweep with an inlet mixture containing 500 ppm NO and 500 ppm H_2. (a) simulation results; (b) experimental measurements.

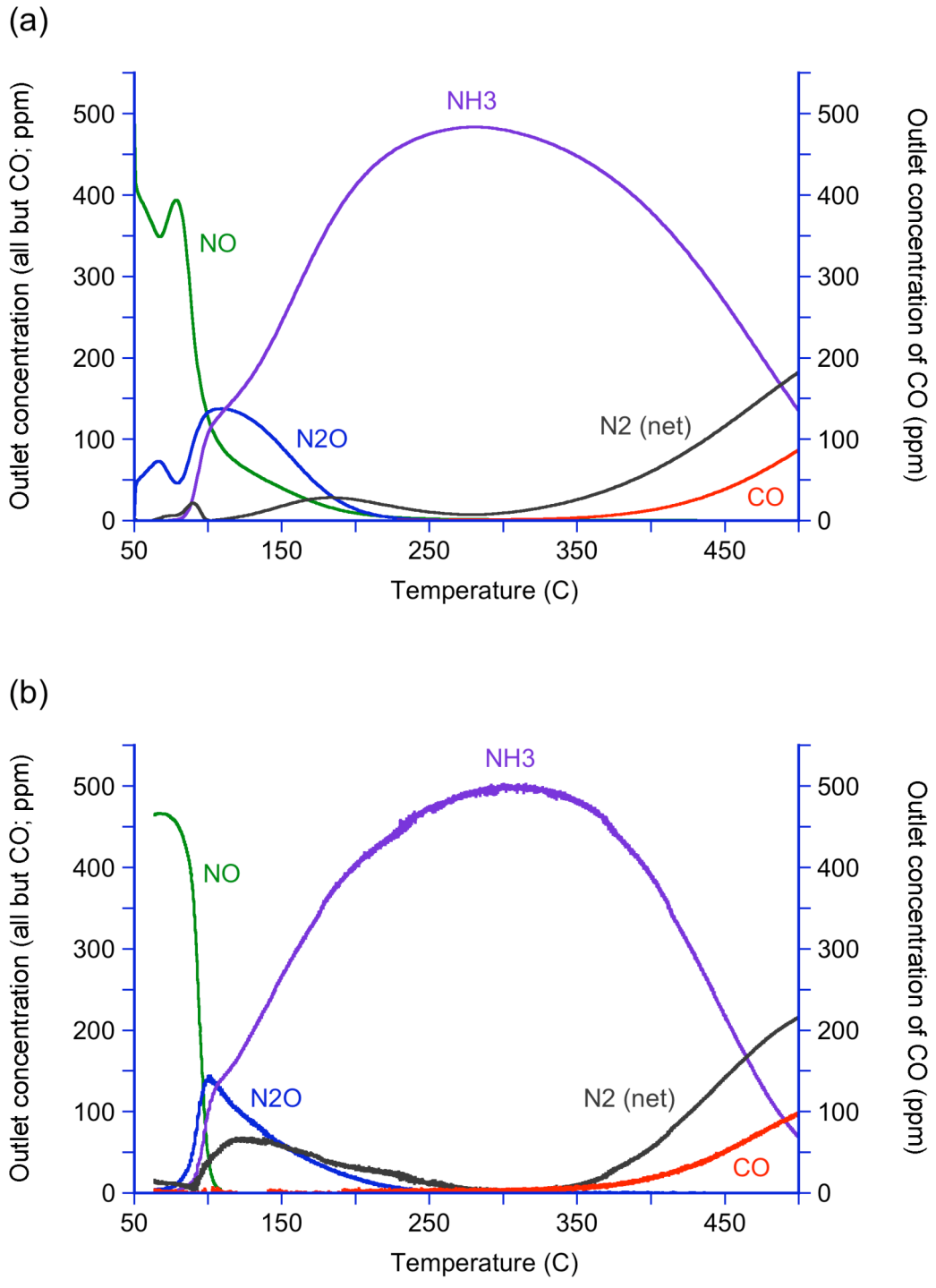

Figure A2. Outlet gas phase concentrations during temperature sweep with an inlet mixture containing 500 ppm NO and 1250 ppm H_2. (a) simulation results; (b) experimental measurements.

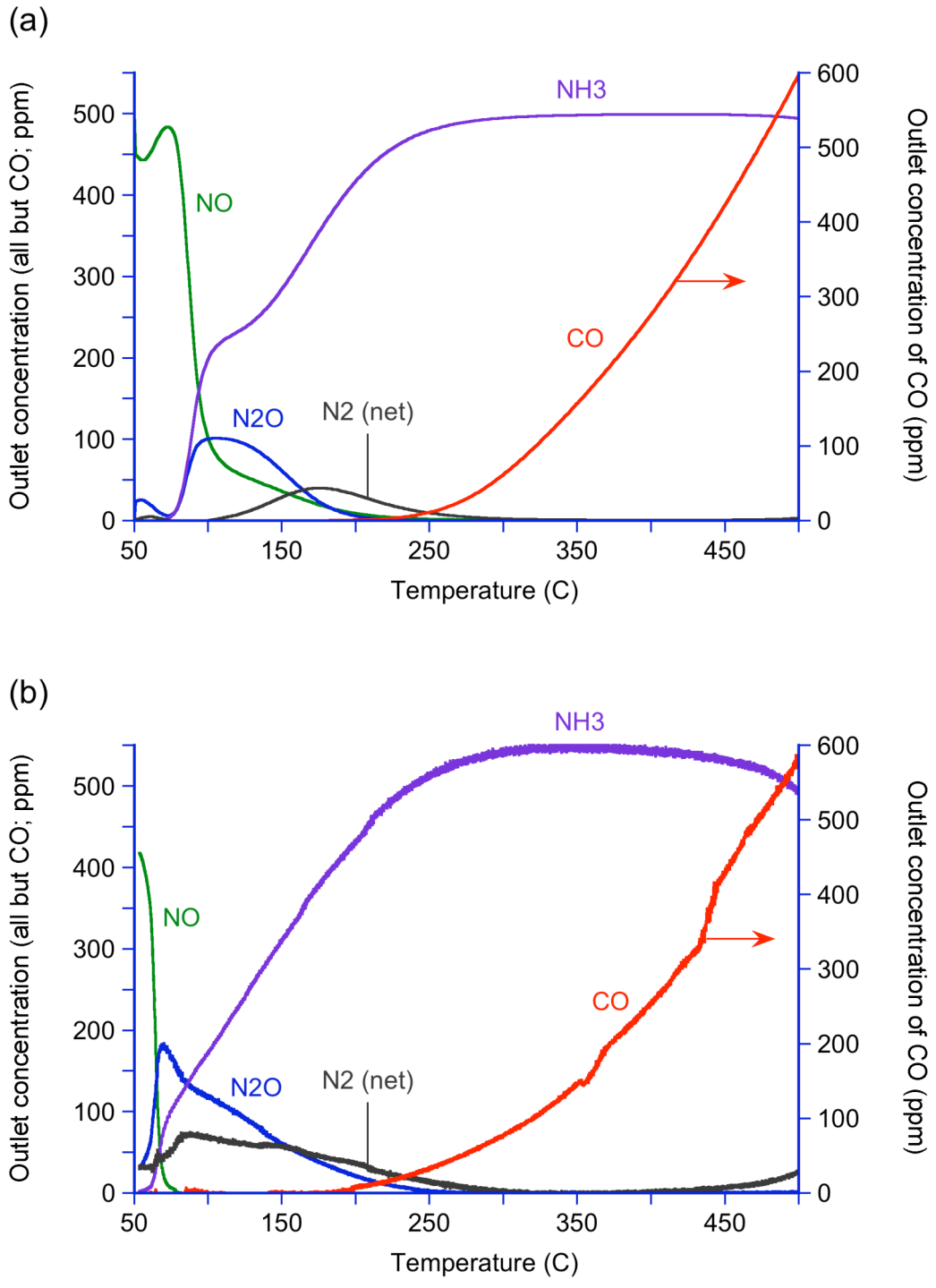

Figure A3. Outlet gas phase concentrations during temperature sweep with an inlet mixture containing 500 ppm NO and 5000 ppm H_2. (a) simulation results; (b) experimental measurements.

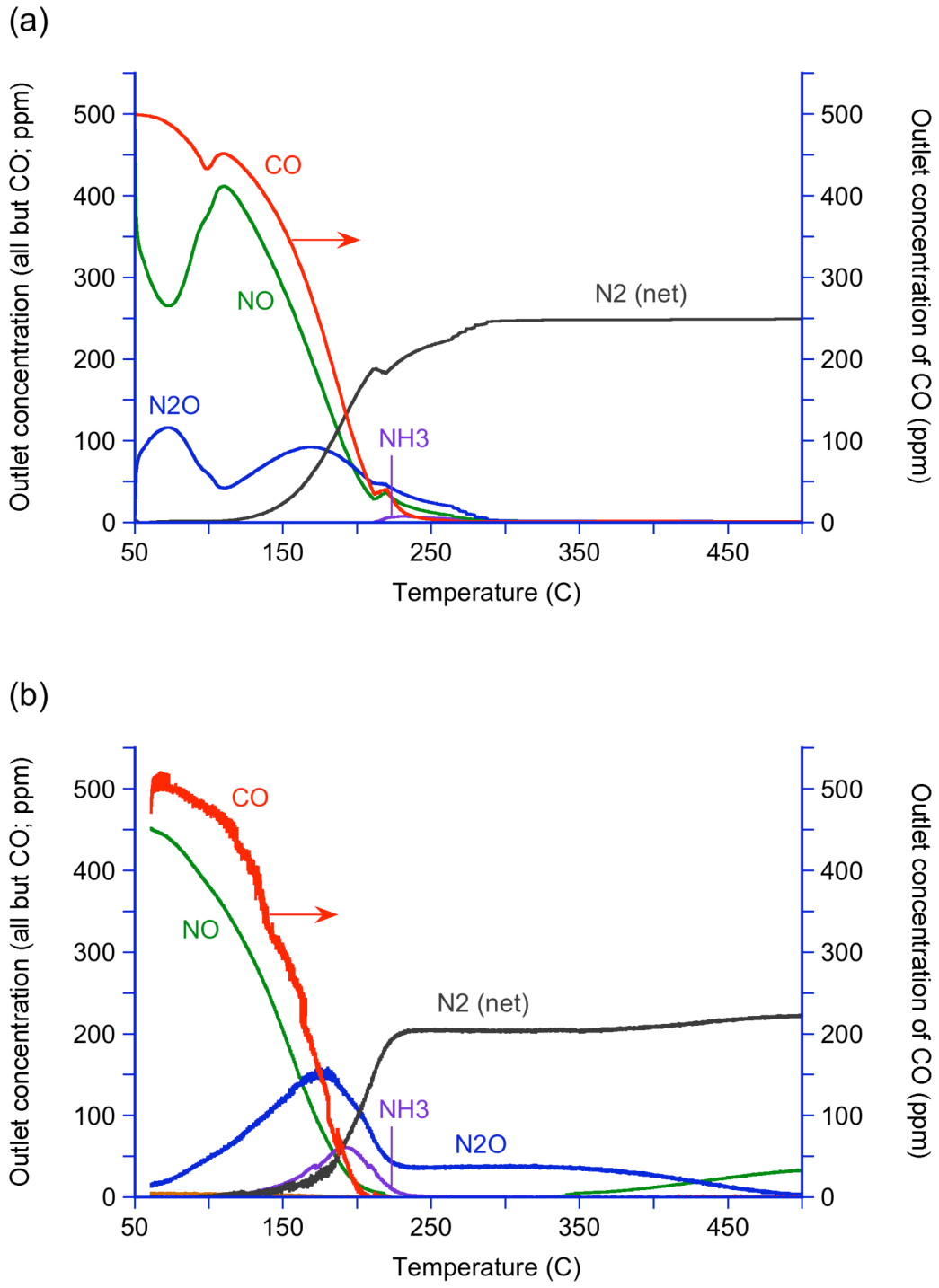

Figure A4. Outlet gas phase concentrations during temperature sweep with an inlet mixture containing 500 ppm NO and 500 ppm CO. (a) simulation results; (b) experimental measurements.

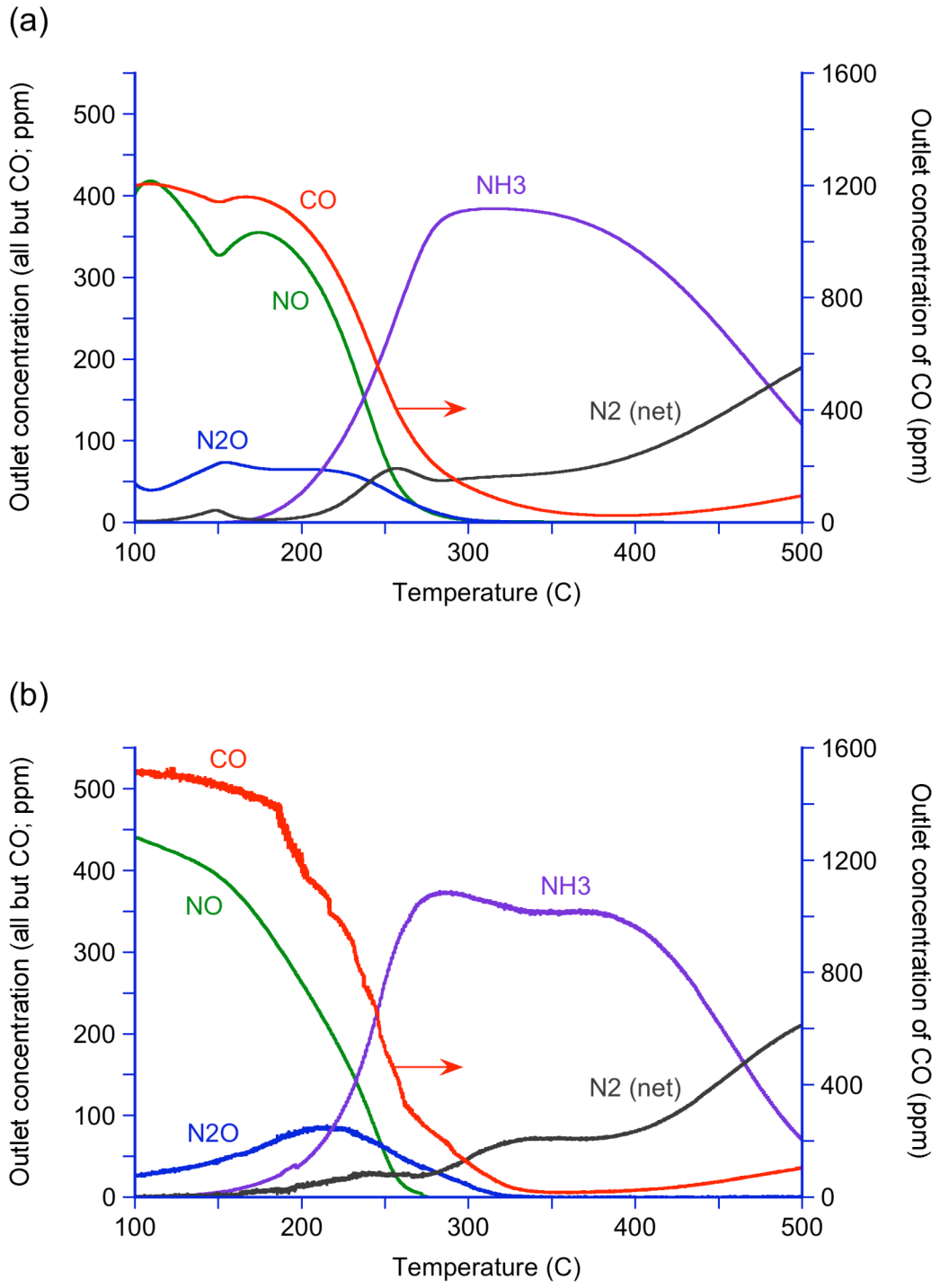

Figure A5. Outlet gas phase concentrations during temperature sweep with an inlet mixture containing 500 ppm NO and 1250 ppm CO. (a) simulation results; (b) experimental measurements.

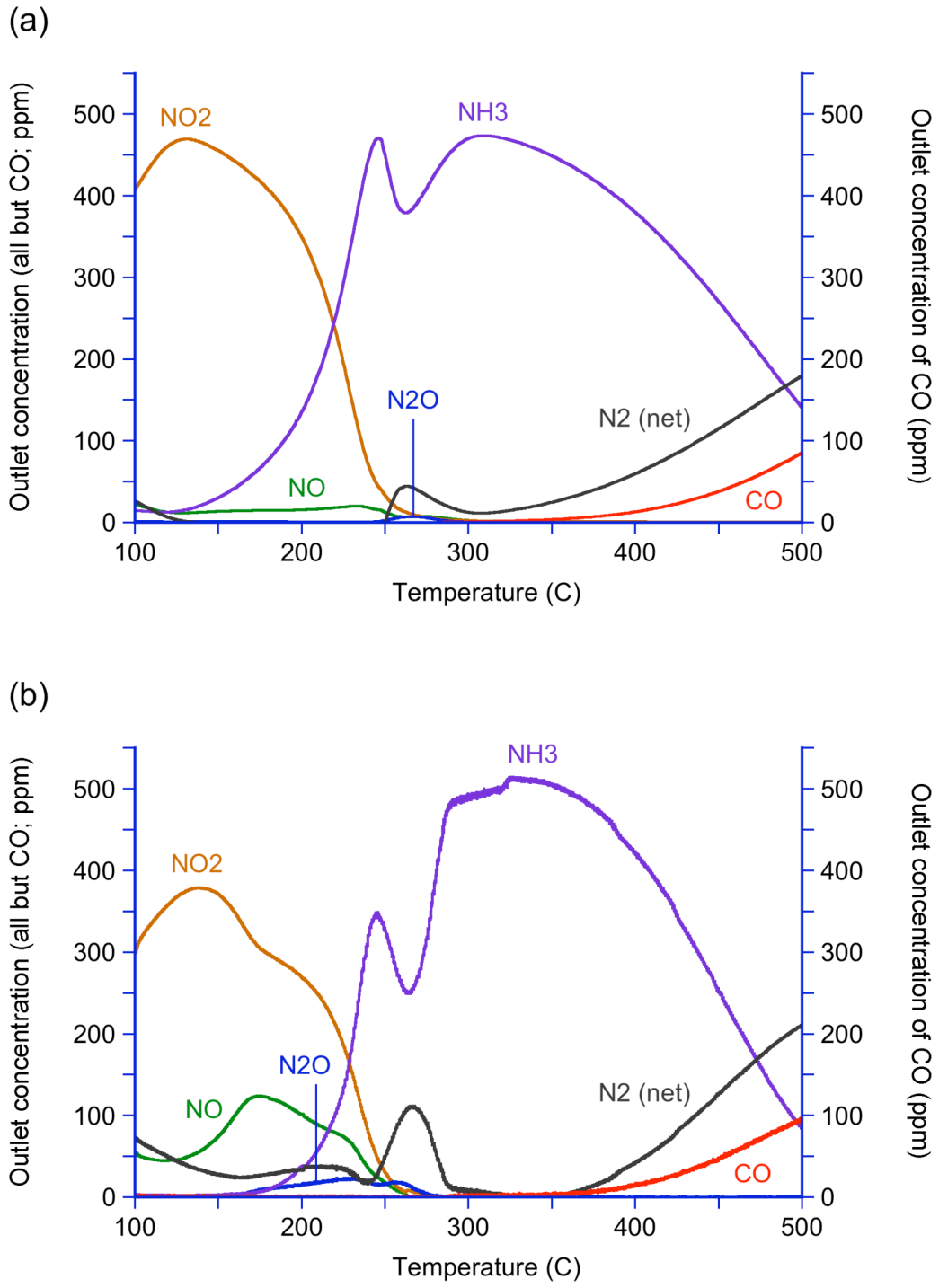

Figure A6. Outlet gas phase concentrations during temperature sweep with an inlet mixture containing 500 ppm NO_2 and 1750 ppm H_2. (a) simulation results; (b) experimental measurements.

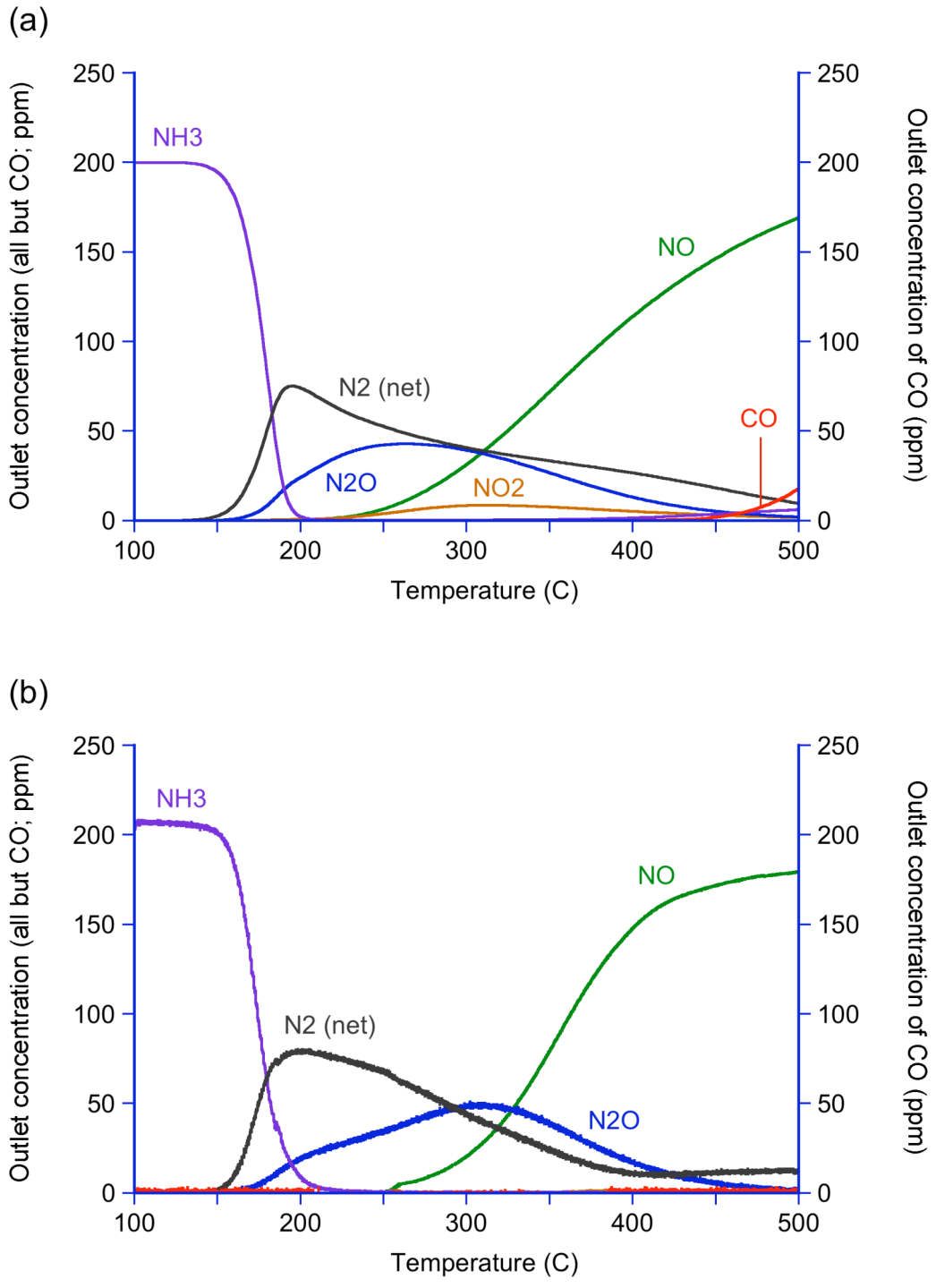

Figure A7. Outlet gas phase concentrations during temperature sweep with an inlet mixture containing 200 ppm NH_3 and 400 ppm O_2. (a) simulation results; (b) experimental measurements.

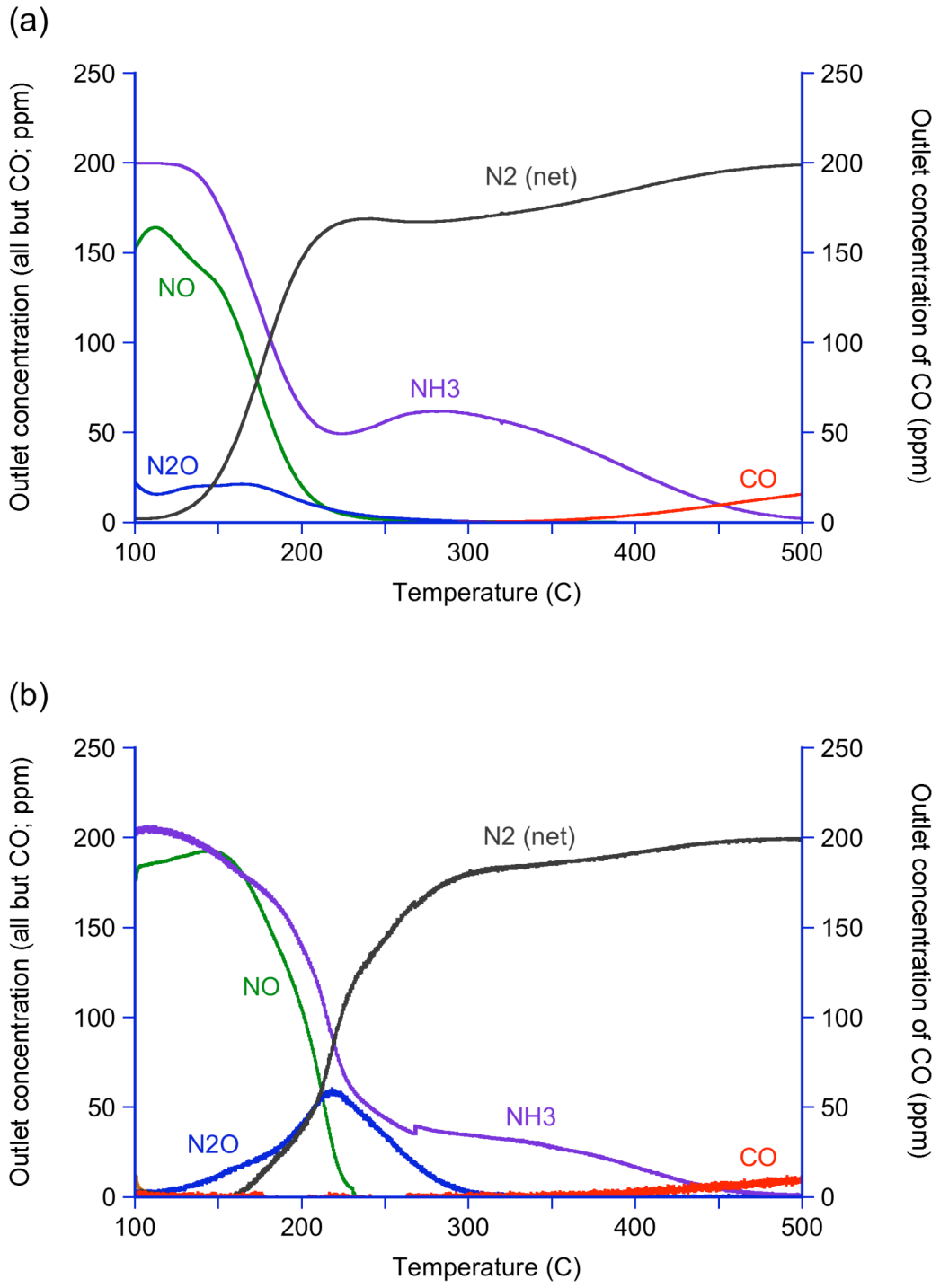

Figure A8. Outlet gas phase concentrations during temperature sweep with an inlet mixture containing 200 ppm NH_3 and 200 ppm NO. (a) simulation results; (b) experimental measurements.

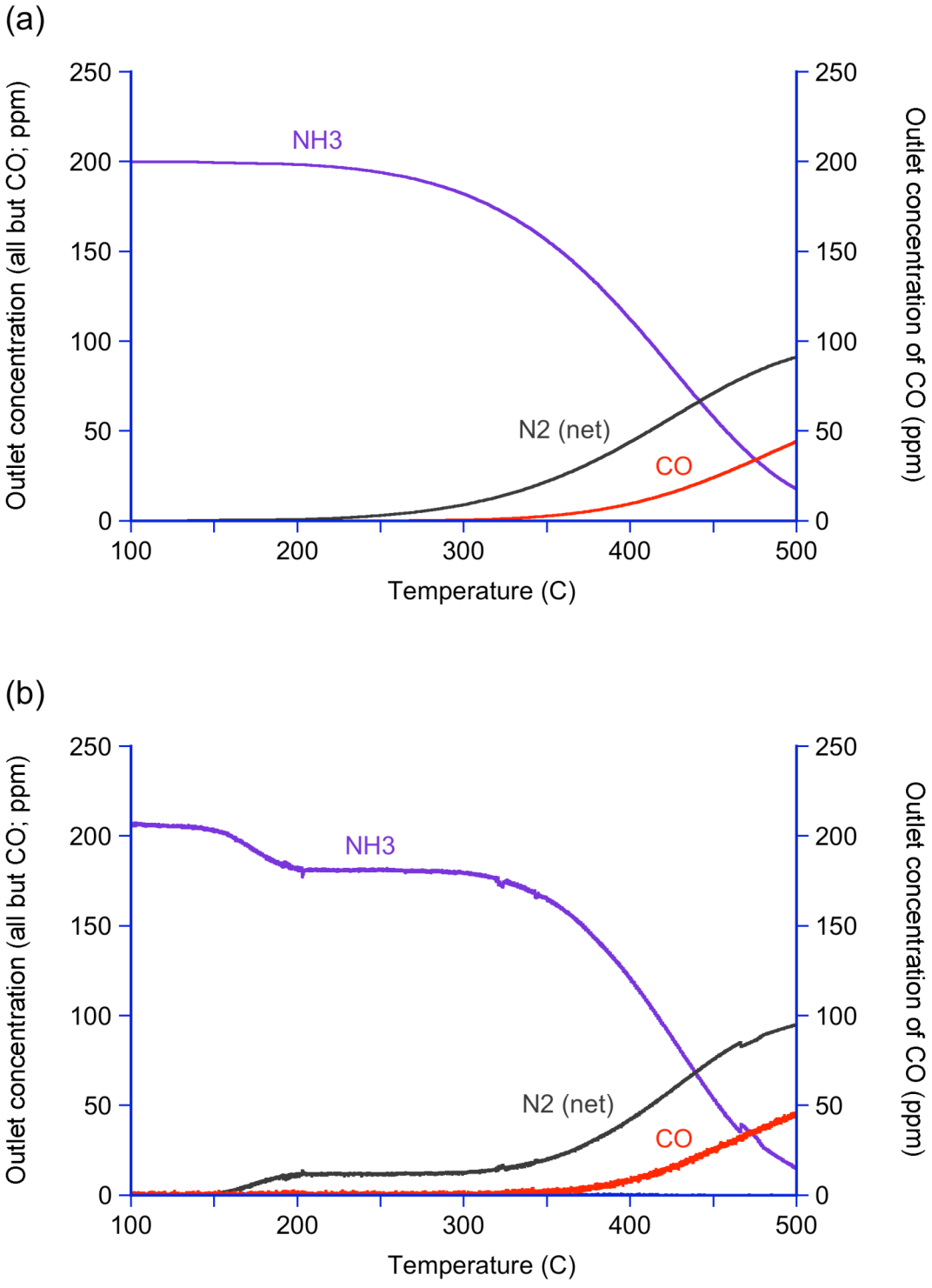

Figure A9. Outlet gas phase concentrations during temperature sweep with an inlet mixture containing 200 ppm NH_3. (a) simulation results; (b) experimental measurements.

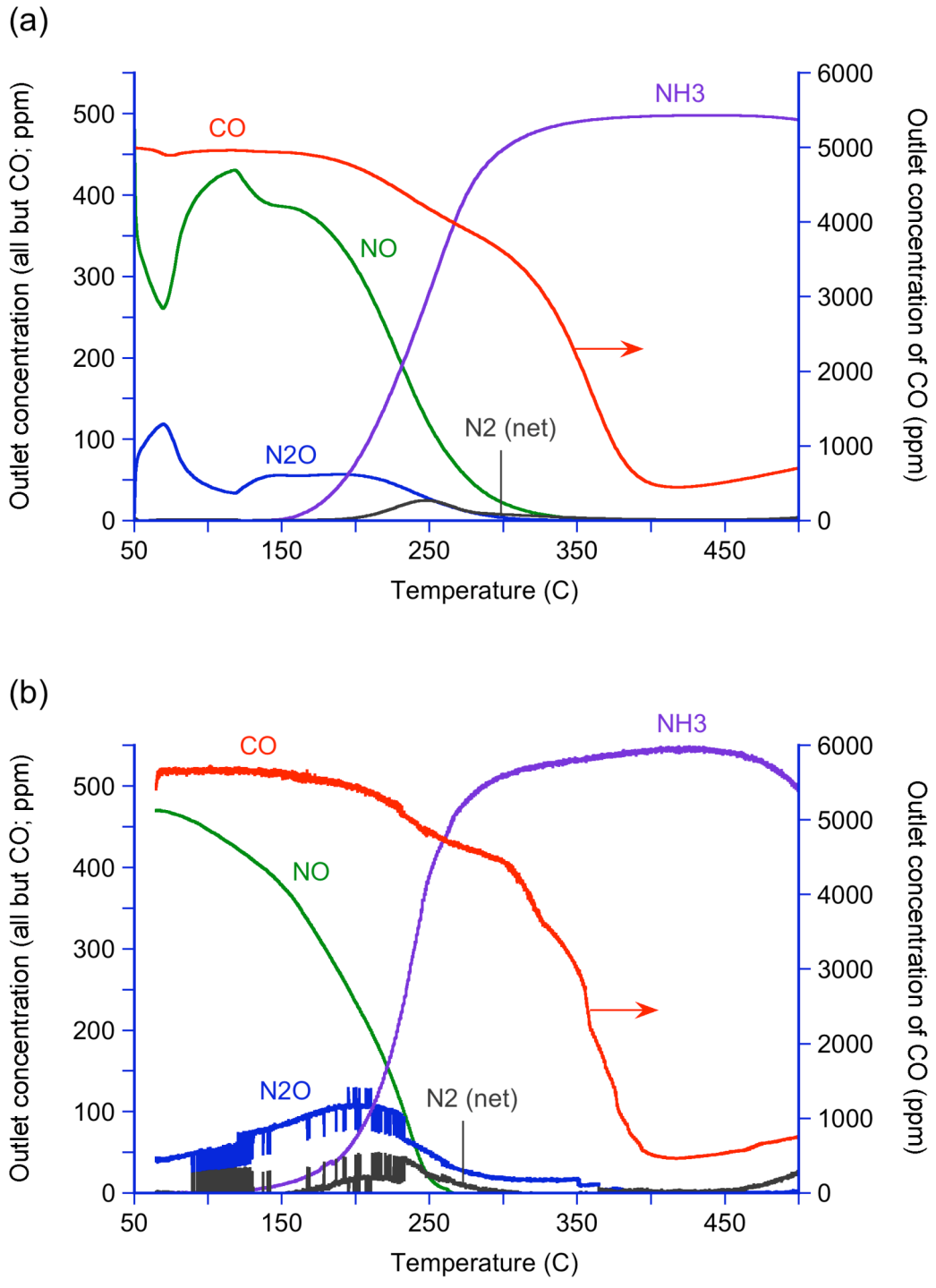

Figure A10. Outlet gas phase concentrations during temperature sweep with an inlet mixture containing 500 ppm NO and 5000 ppm CO. (a) simulation results; (b) experimental measurements.

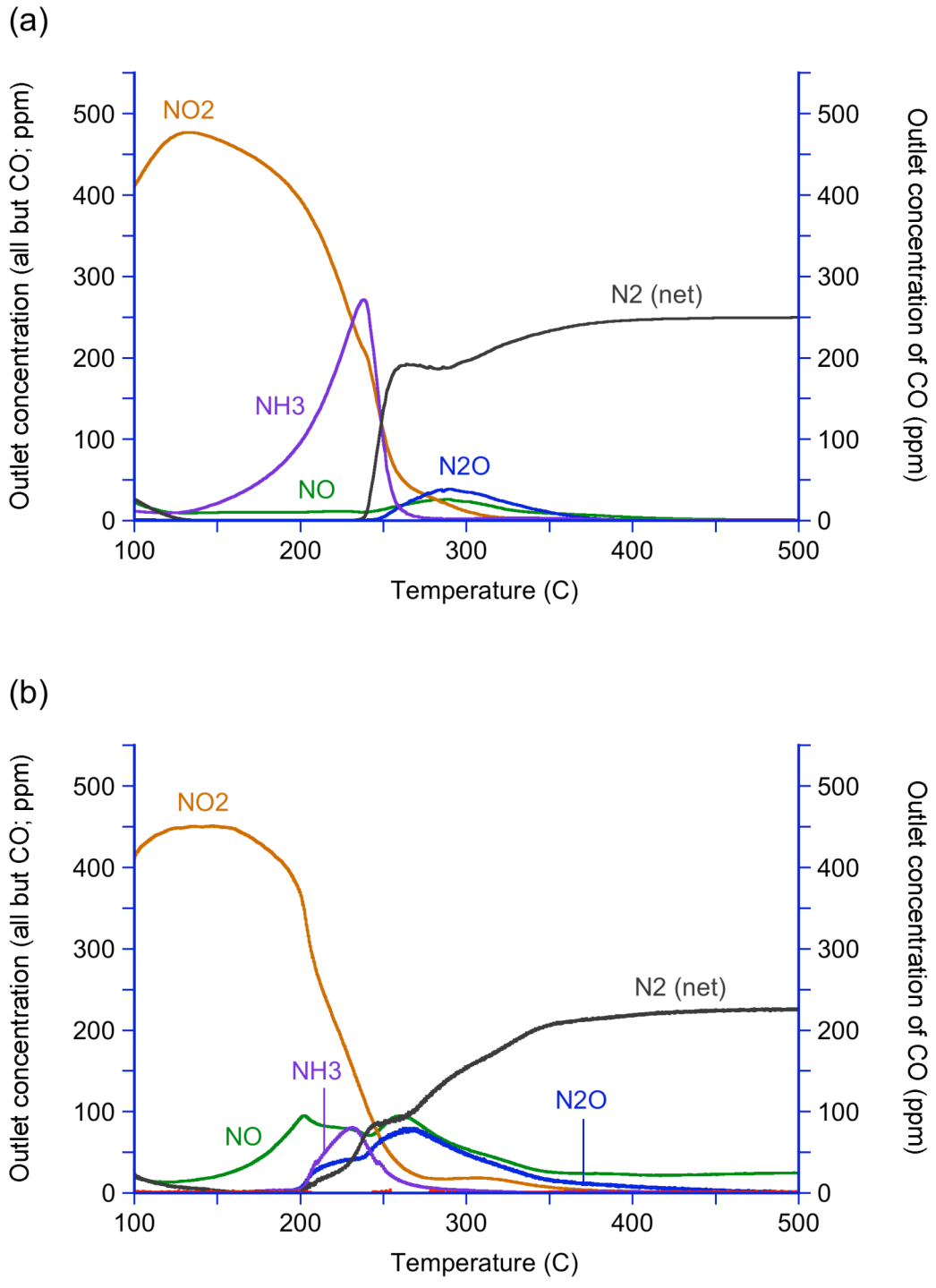

Figure A11. Outlet gas phase concentrations during temperature sweep with an inlet mixture containing 500 ppm NO_2 and 1000 ppm H_2. (a) simulation results; (b) experimental measurements.

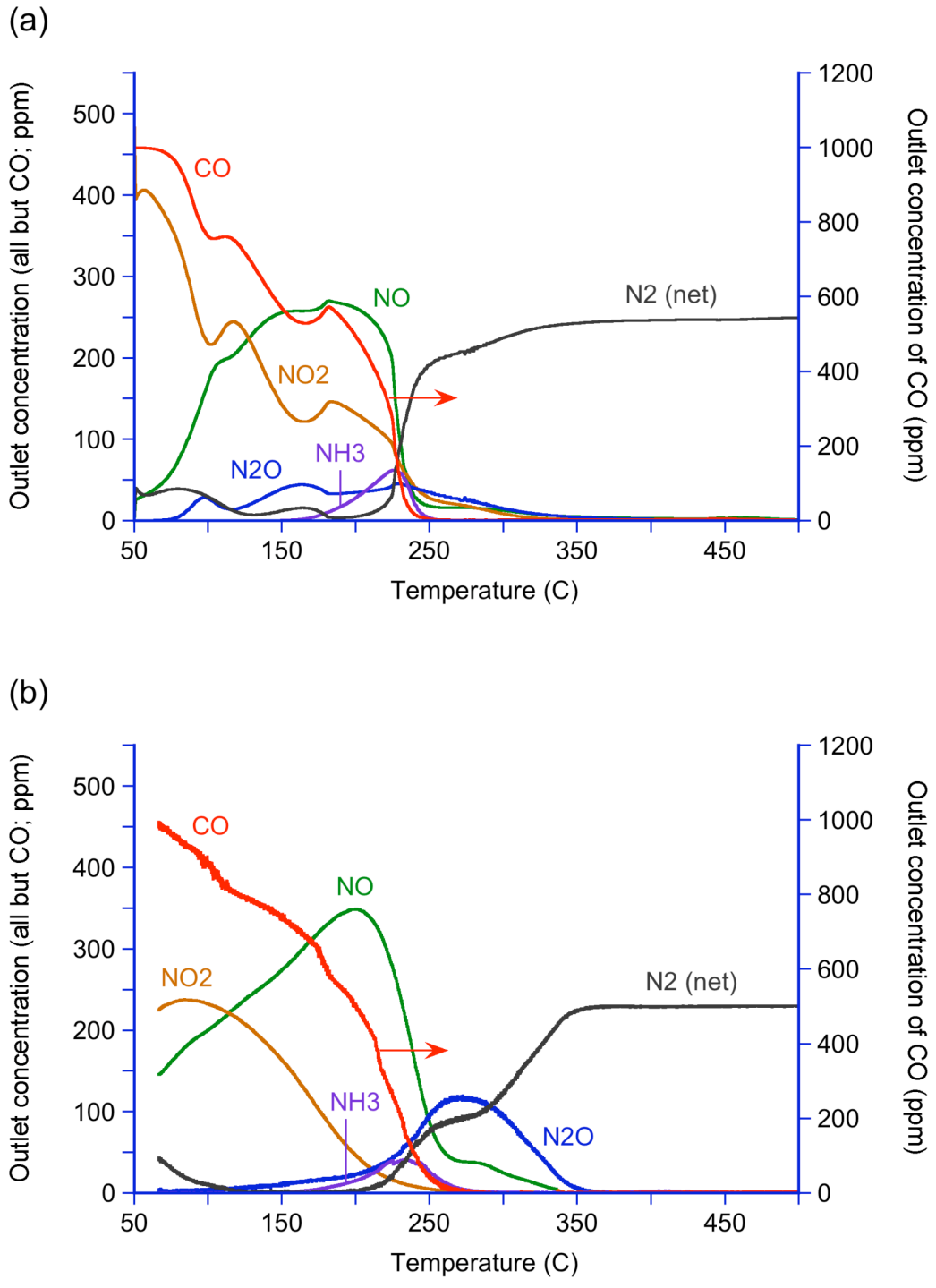

Figure A12. Outlet gas phase concentrations during temperature sweep with an inlet mixture containing 500 ppm NO_2 and 1000 ppm CO. (a) simulation results; (b) experimental measurements.

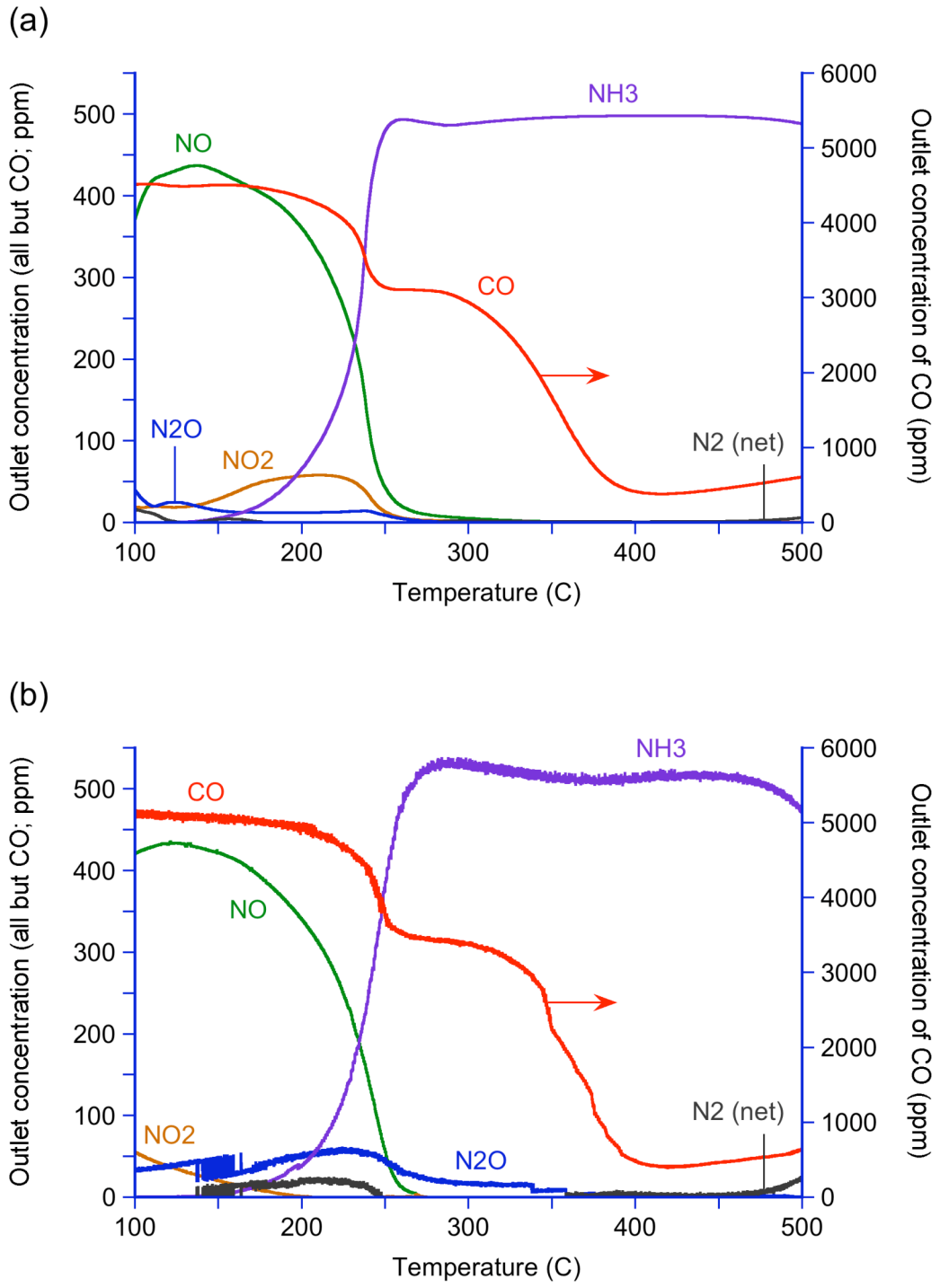

Figure A13. Outlet gas phase concentrations during temperature sweep with an inlet mixture containing 500 ppm NO_2 and 5000 ppm CO. (a) simulation results; (b) experimental measurements.

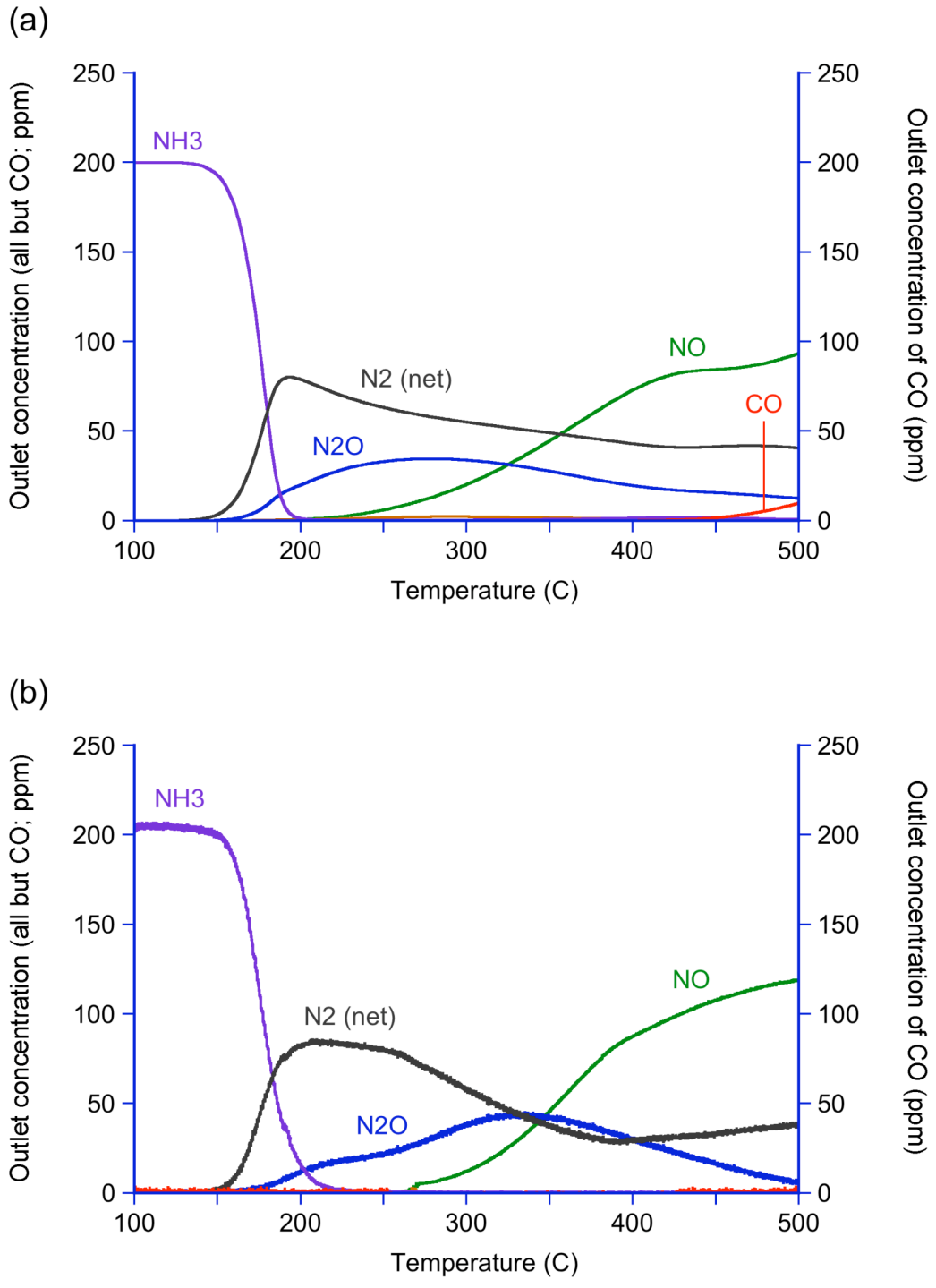

Figure A14. Outlet gas phase concentrations during temperature sweep with an inlet mixture containing 200 ppm NH_3 and 200 ppm O_2. (a) simulation results; (b) experimental measurements.

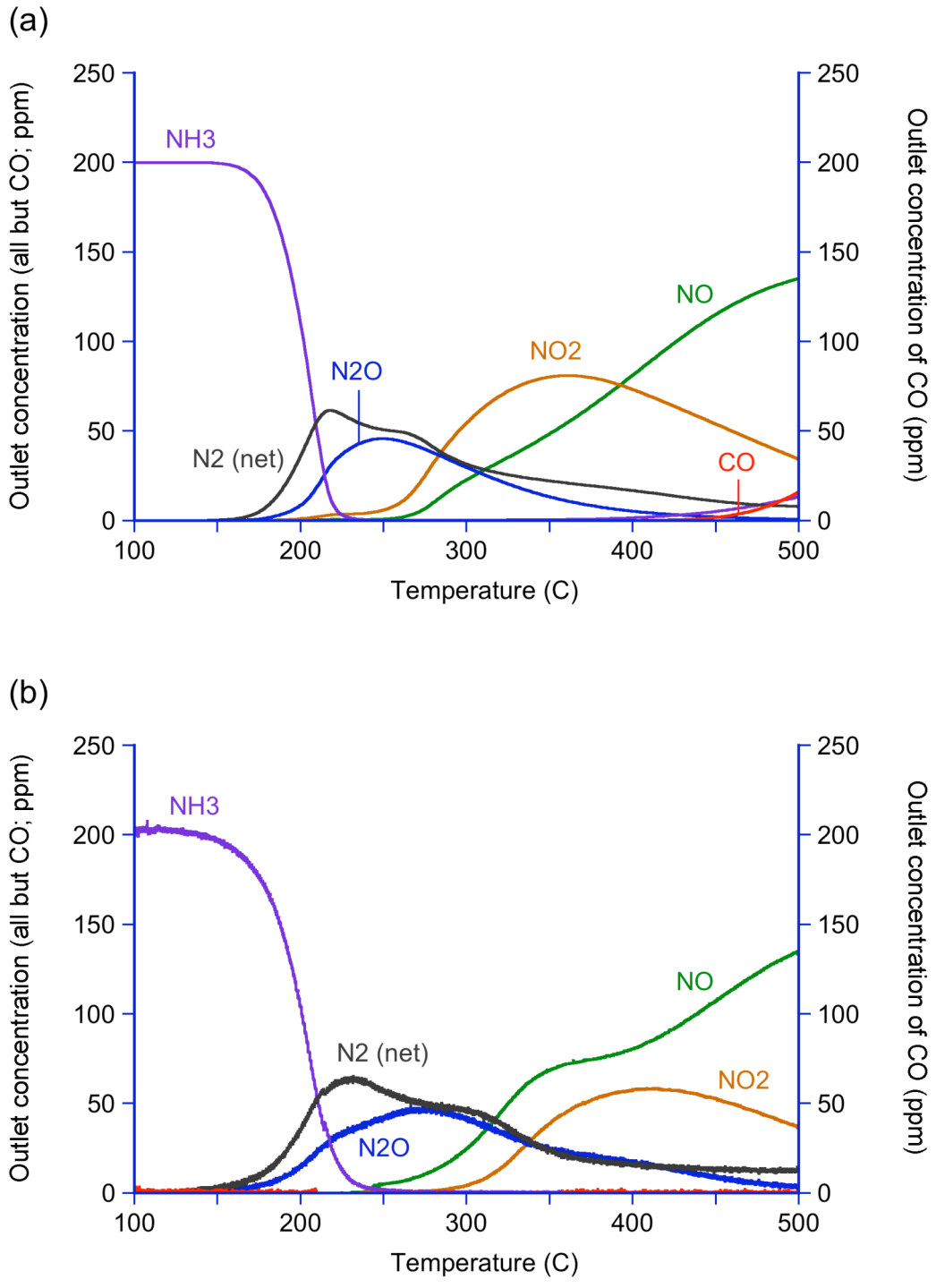

Figure A15. Outlet gas phase concentrations during temperature sweep with an inlet mixture containing 200 ppm NH_3 and 10% O_2. (a) simulation results; (b) experimental measurements.

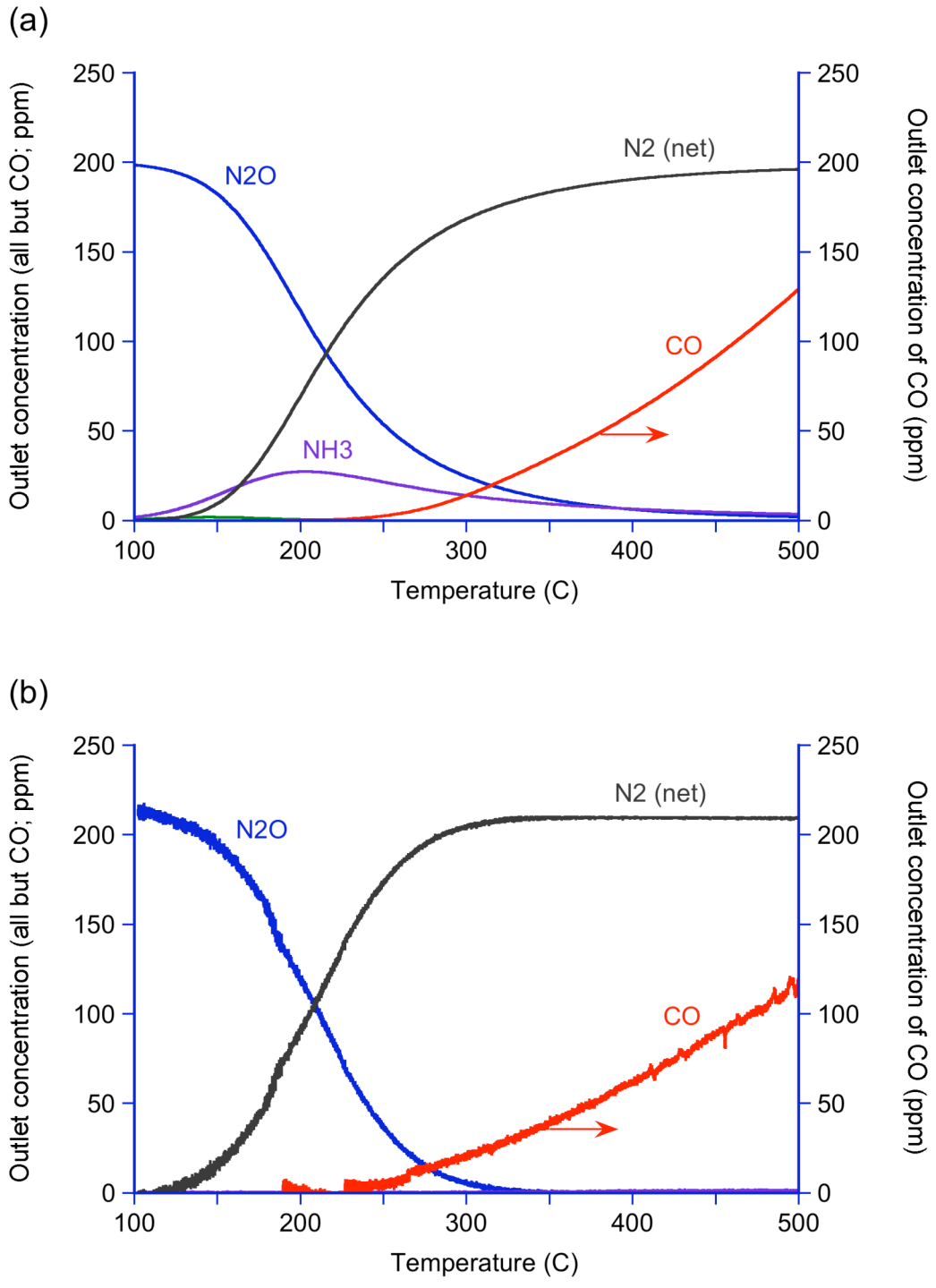

Figure A16. Outlet gas phase concentrations during temperature sweep with an inlet mixture containing 200 ppm N_2O and 1000 ppm H_2. (a) simulation results; (b) experimental measurements.

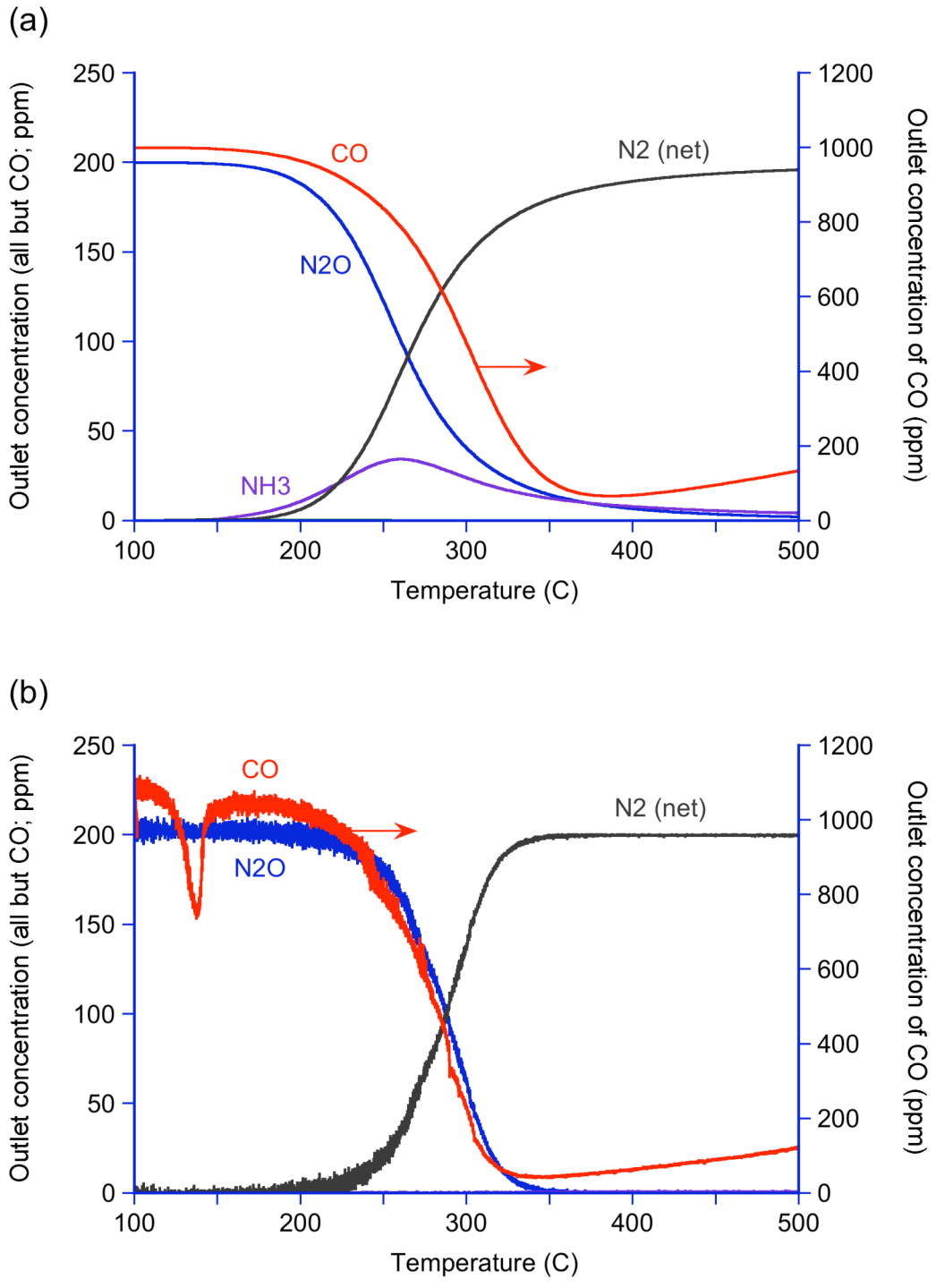

Figure A17. Outlet gas phase concentrations during temperature sweep with an inlet mixture containing 200 ppm N_2O and 1000 ppm CO. (a) simulation results; (b) experimental measurements.

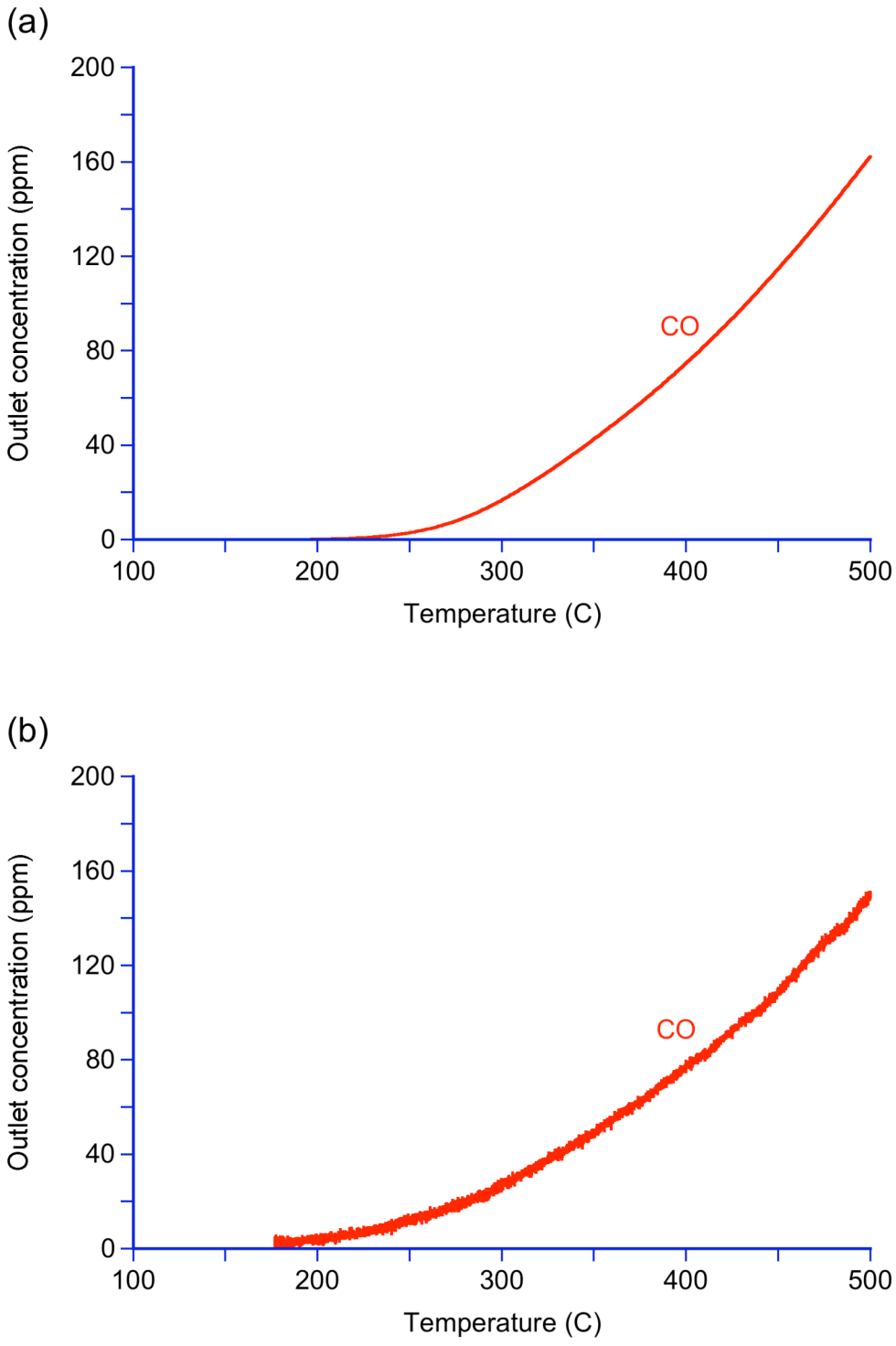

Figure A18. Outlet gas phase concentrations during temperature sweep with an inlet mixture containing 1000 ppm H_2. (a) simulation results; (b) experimental measurements.

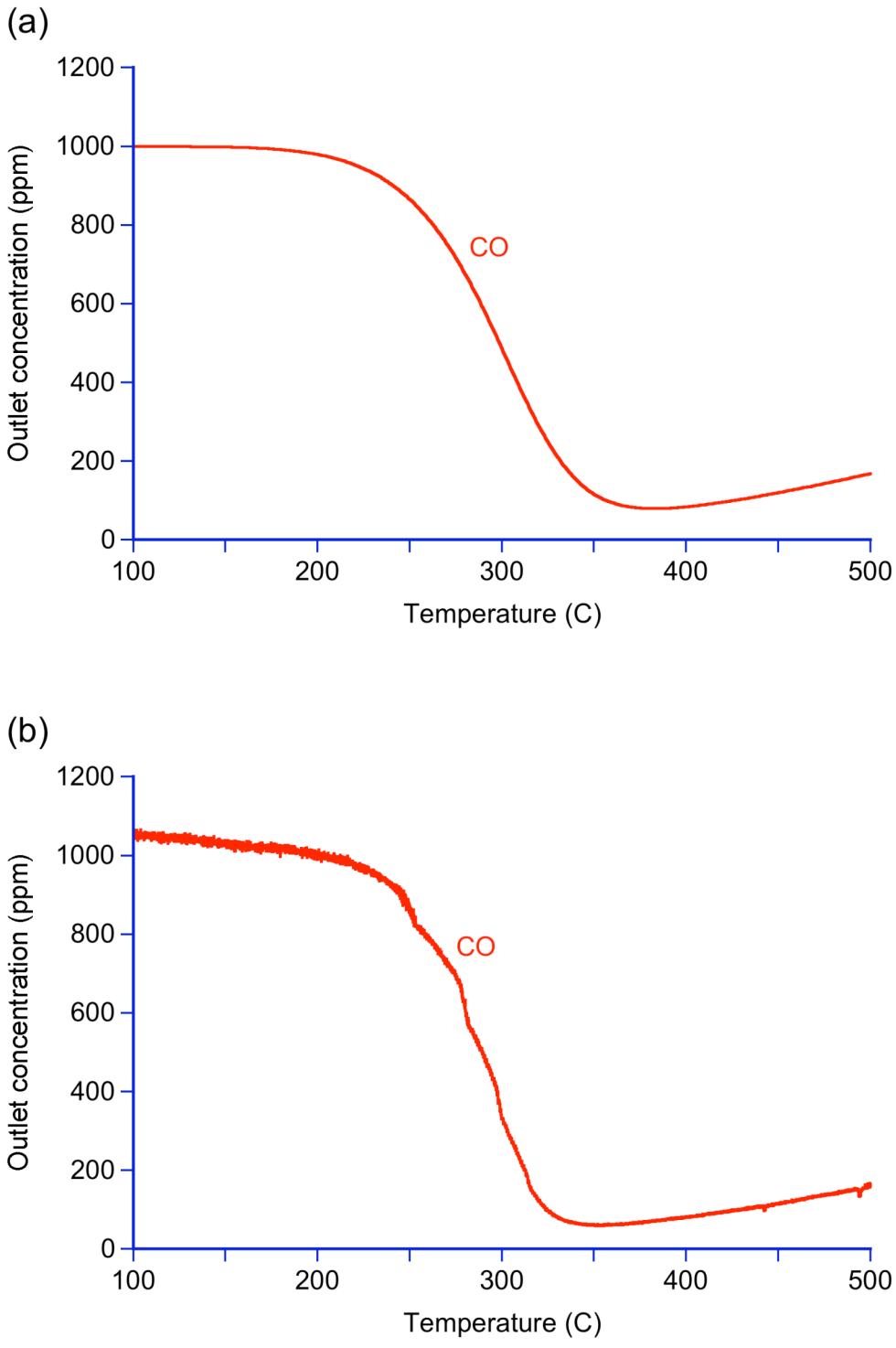

Figure A19. Outlet gas phase concentrations during temperature sweep with an inlet mixture containing 1000 ppm CO. (a) simulation results; (b) experimental measurements.

Distribution

1	MS 0899	Technical Library, 9536
1	MS 9051	N.R. Fornaciari, 8366
1	MS 9052	D.E. Dedrick, 8367
1	MS 9052	A.H. McDaniel, 8367
1	MS 9053	D.L. Siebers, 8362
1	MS 9054	A. McIlroy, 8310
1	MS 9054	A.E. Pontau, 8360


Sandia National Laboratories